MIT Open Access Articles

Impact of Clouds and Hazes on the Simulated JWST Transmission Spectra of Habitable Zone Planets in the TRAPPIST-1 System

Massachusetts Institute of Technology

Impact of Clouds and Hazes on the Simulated *JWST* Transmission Spectra of Habitable Zone Planets in the TRAPPIST-1 System

Thomas J. Fauchez[1,2,3] , Martin Turbet[4,5], Geronimo L. Villanueva[1,3], Eric T. Wolf[6,7], Giada Arney[3,8] ,
Ravi K. Kopparapu[3,8] , Andrew Lincowski[9,10] , Avi Mandell[3,11] , Julien de Wit[12] , Daria Pidhorodetska[8,13] ,
Shawn D. Domagal-Goldman[3,8] , and Kevin B. Stevenson[14,15]

[1] NASA Goddard Space Flight Center, Greenbelt, MD, USA; Thomas.j.fauchez@nasa.gov
[2] Goddard Earth Sciences Technology and Research (GESTAR), Universities Space Research Association, Columbia, MD, USA
[3] GSFC Sellers Exoplanet Environments Collaboration, USA
[4] Laboratoire de Méteorologie Dynamique, IPSL, Sorbonne Universités, UPMC Univ Paris 06, CNRS, 4 Place Jussieu, F-75005 Paris, France
[5] Observatoire Astronomique de l'Université de Genève, Université de Genève, Chemin des Maillettes 51, 1290 Versoix, Switzerland
[6] Laboratory for Atmospheric and Space Physics, Department of Atmospheric and Oceanic Sciences, University of Colorado Boulder, Boulder, CO, USA
[7] NASA Astrobiology Institute's Virtual Planetary Laboratory, Seattle, WA, USA
[8] NASA Goddard Space Flight Center, Greenbelt, MD, USA
[9] Department of Astronomy and Astrobiology Program, University of Washington, Box 351580, Seattle, WA 98195, USA
[10] NASA Astrobiology Institute's Virtual Planetary Laboratory, Box 351580, University of Washington, Seattle, WA 98195, USA
[11] NASA Goddard Space Flight Center, Greenbelt, MD 20771, USA
[12] Department of Earth, Atmospheric and Planetary Sciences, Massachusetts Institute of Technology, Cambridge, MA, USA
[13] University of Maryland Baltimore County/CRESST II, 1000 Hilltop Cir., Baltimore, MD 21250, USA
[14] Space Telescope Science Institute, Baltimore, MD 21218, USA
[15] Johns Hopkins APL, 1100 Johns Hopkins Rd., Laurel, MD 20723, USA

Abstract

The TRAPPIST-1 system, consisting of an ultracool host star having seven known Earth-sized planets, will be a prime target for atmospheric characterization with the *James Webb Space Telescope* (*JWST*). However, the detectability of atmospheric molecular species may be severely impacted by the presence of clouds and/or hazes. In this work, we perform 3D general circulation model (GCM) simulations with the LMD-G model supplemented by 1D photochemistry simulations at the terminator with the Atmos model to simulate several possible atmospheres for TRAPPIST-1e, 1f, and 1g: (1) modern Earth, (2) Archean Earth, and (3) CO_2-rich atmospheres. The *JWST* synthetic transit spectra were computed using the GSFC Planetary Spectrum Generator. We find that the TRAPPIST-1e, 1f, and 1g atmospheres, with clouds and/or hazes, could be detected using *JWST*'s NIRSpec Prism from the CO_2 absorption line at 4.3 μm in less than 15 transits at 3σ or less than 35 transits at 5σ. However, our analysis suggests that other gases would require hundreds (or thousands) of transits to be detectable. We also find that H_2O, mostly confined in the lower atmosphere, is very challenging to detect for these planets or similar systems if the planets' atmospheres are not in a moist greenhouse state. This result demonstrates that the use of GCMs, self-consistently taking into account the effect of clouds and subsaturation, is crucial to evaluate the detectability of atmospheric molecules of interest, as well as for interpreting future detections in a more global (and thus robust and relevant) approach.

Unified Astronomy Thesaurus concepts: Radiative transfer (1335)

1. Introduction

During the last decade, a rapidly increasing number of Earth-sized planets in the so-called habitable zone (HZ) have been discovered. Among the most famous of them are Kepler-186f (Quintana et al. 2014), Proxima Centauri b (Anglada-Escudé et al. 2016), GJ 1132b (Berta-Thompson et al. 2015), Ross 128b (Bonfils et al. 2018), and the TRAPPIST-1 system (Gillon et al. 2016, 2017b). The HZ is defined as the region around a star where a planet with appropriate atmospheric pressure, temperature, and composition can maintain liquid water on its surface (Kasting et al. 1993; Selsis et al. 2007; Kopparapu et al. 2013, 2017; Yang et al. 2014), which is crucial for life as we know it. However, the abundant presence of liquid water at the surface of a planet is not the only criterion that deems it to be habitable. The planet's geophysics and geodynamics, as well as its interaction with its host stars' plasma and radiation environment, are also crucial parameters to determine its habitability (Lammer et al. 2009). Low-mass stars (late K and all M dwarf stars) provide the best opportunity for detecting

and characterizing habitable terrestrial planets in the coming decade. The small size of these stars allows for a greater chance of detection of terrestrial-sized planets, and planets in their compact HZ, which orbit more frequently, lead to a better signal-to-noise ratio (S/N) level than planets orbiting in the HZ of Sun-like stars. For late M dwarfs, such as TRAPPIST-1 (M8V), the S/N can be amplified by a factor of up to 3 compared to stars with types earlier than M1 (de Wit & Seager 2013). Among the most promising systems with planets in the HZ of low-mass stars is the nearby TRAPPIST-1 system, located 12 pc away, discovered by Gillon et al. (2016, 2017b) and Luger et al. (2017) and composed of at least seven rocky planets, with three of them in the HZ. The system's host star, TRAPPIST-1, is an active late M dwarf (O'Malley-James & Kaltenegger 2017; Wheatley et al. 2017; Vida & Roettenbacher 2018) whose stellar flares could bathe the planetary environment with high-energy radiation and plasma, creating severe obstacles to retaining an atmosphere or sustaining habitable conditions on their surface. Despite these difficult conditions, Bolmont et al. (2017), Bourrier et al. (2017), and Dong et al. (2018) have argued

that the TRAPPIST-1 planets could retain surface liquid water if they were formed with abundant initial water endowment. Transit-timing variation measurements of the TRAPPIST-1 planets by Grimm et al. (2018) have also suggested a volatile-rich composition and thus a potentially large amount of water.

The proximity of the TRAPPIST-1 system and the high frequency of its planetary transits make it a prime target for temperate rocky exoplanet atmospheric characterization. The first atmospheric characterization with the *Hubble Space Telescope* (*HST*) by de Wit et al. (2016, 2018) revealed that the TRAPPIST-1 planets do not contain a cloud-/haze-free H_2-dominated atmosphere but may instead be composed of a wide variety of atmospheres dominated by N_2, O_2, H_2O, CO_2, or CH_4. Following these studies, Moran et al. (2018) used lab measurements and a 1D atmospheric model to show that H_2-dominated atmospheres with clouds/hazes would better fit the spectra than clear-sky H_2-dominated atmospheres (except for TRAPPIST-1g). However, the noise on the *HST* transmission spectra is on the order of hundreds of parts per million (ppm; de Wit et al. 2018). The sensitivity, spectral resolution, and wide wavelength coverage of the future *James Webb Space Telescope* (*JWST*) will be needed to address whether or not these planets have an atmosphere and uncover clues related to their composition (Barstow & Irwin 2016; Morley et al. 2017).

Before *JWST* observes these planets, it is important to understand the possible composition of their atmospheres (if any) and their climate conditions. The 3D general circulation models (GCMs) are the most sophisticated tools to address these questions because they can simulate tidally locked planets, and they allow for a self-consistent and coupled treatment of all physical processes occurring in a planetary atmosphere. This is particularly important for water in its various thermodynamic phases, which is responsible for water vapor greenhouse feedback and the sea ice albedo. Both are strong and positive effects amplifying temperature perturbations to the climate system in either direction. The interaction between water vapor and the 3D atmospheric dynamics controls the relative humidity of the atmosphere and, ultimately, the strength of a planet's water vapor greenhouse effect (Pierrehumbert 1995). Similarly, the spatial distributions of sea ice, snow coverage, and clouds largely determine the planetary albedo.

The 1D (vertical) models struggle to simulate rocky planets within the HZs of low-mass stars (late K and all M dwarfs) in synchronous rotation (Leconte et al. 2015; Barnes 2017), yet it is precisely these planets, such as the TRAPPIST-1 system, that have deep transits and shorter orbits that allow for near-term atmospheric characterization (Kaltenegger & Traub 2009; Snellen et al. 2013) with *JWST* or future ground-based observatories such as E-ELT, GMT, or TMT. In this situation, one side of the planet is permanently exposed to starlight, while the other side is condemned to permanent darkness. Tidally locked planets in the HZs of low-mass stars usually have rotation periods that are much longer than that of Earth, leading to a weaker Coriolis force. Instead of having primarily zonal flows with midlatitude jets like on Earth, modeling studies suggest that these planets have substellar to antistellar radial flow aloft, with strong rising motions on the permanent dayside and subsiding motions on the permanent nightside (Joshi 2003; Merlis & Schneider 2010). Only 3D climate models can capture these motions that have strong effects on the climate system. Yang et al. (2013) showed that slow and synchronously rotating

planets have thick clouds near the substellar point, drastically increasing the planetary albedo and inhibiting the planet from entering a runaway greenhouse state even at much higher incident stellar fluxes compared to an Earth–Sun twin. The 3D models have also been used to study the spatial variability of chemical species of rocky exoplanets and have found that significant chemical gradients exist between the daysides and nightsides of slow-rotating planets (Chen et al. 2018). Finally, several studies (Hu & Yang 2014; Way et al. 2017; Del Genio et al. 2019) have shown the importance of accounting for ocean heat transport (OHT) for slow-rotating habitable planets. Each of these processes has a great impact on a planet's climate and can only be adequately portrayed through the use of 3D models. However, 3D models require a larger set of initial and boundary conditions, which are not well known for exoplanets, while simpler but faster 1D models can explore a larger parameter space; therefore, the two approaches are complementary.

Some 3D GCM simulations of the TRAPPIST-1 planets have already been performed. Wolf (2017) and Turbet et al. (2018) showed that TRAPPIST-1e is the most likely planet to be habitable, based on the result that it can retain liquid water on its surface for a large set of atmospheric compositions and thicknesses. Moreover, results suggest that a few bars of surface CO_2 are needed to maintain ice-free surfaces on TRAPPIST-1f and 1g. Grimm et al. (2018) found that while TRAPPIST-1e may have a large rocky interior, TRAPPIST-1f and 1g are likely to be volatile-rich. Note that 1D climate model simulations have also been used for TRAPPIST-1 planets (Morley et al. 2017; Lincowski et al. 2018; Lustig-Yaeger et al. 2019) with the limitations of this approach described earlier. For instance, in their simulated transmission spectra, Morley et al. (2017) considered clear-sky atmospheres, while it is not realistic when H_2O or CO_2 are in the atmosphere and could eventually form clouds, or CH_4 and H_2SO_4, which could form organic and sulfuric hazes. In Lincowski et al. (2018), water cloud optical thicknesses were not used consistently with the water vapor mixing ratio. Lustig-Yaeger et al.'s (2019) results suggest that NIRSpec is the most favorable *JWST* instrument to characterize the atmospheres of TRAPPIST-1 planets and only a few transits would be needed to detect CO_2.

Clouds or other aerosols, such as photochemical hazes, could have a large impact on both the climate and the detectability of spectral features through transmission spectroscopy. Atmospheric conditions favoring the presence of clouds and/or hazes could severely impact the observed transmission spectra by flattening spectral lines. This phenomenon has been shown to be widespread in observations of larger planets with clouds, such as super-Earth GJ 1214b (Kreidberg et al. 2014), gaseous giant WASP-12b (Wakeford et al. 2017), and WASP-31b (Sing et al. 2016). It has also been observed for hazes, for example, on WASP-6b (Nikolov et al. 2015) and HAT-P-12b (Sing et al. 2016). Furthermore, Arney et al. (2017) simulated *JWST* observations for a hazy Archean Earth orbiting around the M4 dwarf star GJ 876 using the Deming et al. (2009) *JWST* simulator. The spectra were computed with an atmospheric model coupled to the spectral mapping atmosphere radiative transfer model (Meadows & Crisp 1996). They showed that the hazes flatten the spectrum and reduce the relative spectral impact of gaseous absorption in the *JWST* NIRISS bandpass. Hazes can significantly impact *JWST* spectra, and accounting

for them can improve the observational strategies of potentially haze-rich worlds.

In this paper, we use a 3D GCM adapted for the TRAPPIST-1 planets (Turbet et al. 2018) to explore how aerosol formation, including H_2O liquid and ice clouds, CO_2 clouds, and photochemical organic hazes impact the atmospheres and simulated transmission spectra of TRAPPIST-1e, 1f, and 1g, with a focus here on the scenarios where these planets are habitable. The TRAPPIST-1 system is a natural laboratory for studying haze and cloud formation because the planets receive a wide range of incident stellar fluxes. Therefore, the results of our study can be applied to a wide range of Earth-sized planets orbiting M dwarfs. Hazes and clouds are notoriously difficult to model in 1D, which motivated us to use a GCM in this work. However, the chemistry that impacts cloud and haze formation is difficult to simulate in 3D, mainly because it requires a large amount of computing time. To date, the best solution is a nested set of models that leverage the ability of 1D models to simulate photochemistry/hazes and the ability of 3D GCMs to simulate clouds. In this work, we have sequentially connected (i) the 3D GCM simulations accounting for cloud formation with (ii) a 1D radiative-convective photochemical model accounting for the formation of hazes, along with (iii) a transit transmission spectra generator to model *JWST* observations.

The main purpose of this paper is to explore whether and how clouds and photochemical hazes can affect our ability to characterize the atmospheric composition of habitable planets around TRAPPIST-1. We chose to explore three main types of habitable planet atmospheres, representative of habitable planets known to exist and to have existed in the solar system.

1. Modern Earth. This is the best example we have of a habitable planet. It is also the most widespread benchmark for habitable planets in the literature (Barstow & Irwin 2016; Morley et al. 2017; Lincowski et al. 2018).
2. Archean Earth. This case is representative of the early Earth (during the Archean epoch), at a time when Earth had oceans of liquid water, despite a different atmosphere (i.e., both CO_2- and CH_4-rich) from today's. For this case of a habitable planet, we used different scenarios of Archean atmospheres from Charnay et al. (2013).
3. Planet with a thick CO_2-dominated atmosphere. This case is likely representative of the early Earth (during the Hadean epoch), early Venus, and early Mars, at a time when Martian valley networks and lakes were formed (Haberle et al. 2017; Kite 2019).

The paper is structured as follows. Section 2 discusses the method and tools used in this study to simulate both the climate and the transmission spectra of TRAPPIST-1 planets in the HZ. Sections 3–5 successively present the climate and *JWST* transmission spectra for the three types of habitable planets introduced above (modern Earth, Archean Earth, and planets with a thick CO_2-dominated atmosphere). The sections have been ordered by degree of complexity. In Section 3, we focus on simulated atmospheres with boundary conditions based on the modern Earth, highlighting the effect of clouds and photochemical molecular species. In Section 4, we focus on simulated atmospheres based on Archean Earth boundary conditions, highlighting the effect of clouds, photochemical molecular species, and photochemical hazes. In Section 5, we focus on CO_2-dominated atmospheres, highlighting the effect of H_2O and CO_2 clouds. Discussions of our results are provided in Section 6, with a particular emphasis on the detectability of H_2O. Finally, conclusions and perspectives are presented in Section 7.

2. Method: From Climate to Spectra

2.1. Simulation of the Climate

The Laboratoire de Météorologie Dynamique Generic (LMD-G; Wordsworth et al. 2011) model is the (exo)planetary version of the Laboratoire de Métérologie Dynamique zoom (LMDz), a GCM historically built using Mars (Forget et al. 1999) and Earth (Hourdin et al. 2006) LMD GCMs. This is a versatile GCM, able to handle a wide range of temperatures and surface pressures, as well as various condensates (e.g., H_2O, CO_2, CH_4, N_2). Numerous studies have taken advantage of the GCM's versatility to model planetary atmospheres in the solar system and beyond (Wordsworth et al. 2011, 2013, 2015; Charnay et al. 2013, 2015a, 2015b; Leconte et al. 2013a, 2013b; Turbet et al. 2016, 2017a, 2017b, 2018; Bolmont et al. 2017).

2.1.1. Radiative Transfer

The LMD-G uses a generalized radiative transfer algorithm for absorption and scattering by the atmosphere, clouds, and surface from the far-infrared to visible range (Wordsworth et al. 2011). The scattering effects of the atmosphere and clouds are parameterized through a two-stream scheme (Toon et al. 1989) using the method of Hansen & Travis (1974). Absorption coefficients are computed with the correlated k-distribution method (Lacis & Oinas 1991) using absorption lines from HITRAN 2008 (Rothman et al. 2009). The collision-induced and dimer absorptions (Wordsworth et al. 2010; Richard et al. 2012) and sub-Lorentzian profiles (Perrin & Hartmann 1989) were computed as in Charnay et al. (2013) and Wordsworth et al. (2013). Present-day Earth, Archean Earth, and CO_2-dominated atmosphere absorption coefficients were computed as in Leconte et al. (2013a), Charnay et al. (2013), and Wordsworth et al. (2013), respectively. Between 36 and 38 spectral bands are considered in the shortwave and 32 and 38 in the longwave ranges. Sixteen nonregularly spaced grid points were adopted for the g-space integration, with "g" the cumulative distribution function of the absorption data for each band.

TRAPPIST-1 emission spectra were computed using the synthetic BT-Settl spectrum (Rajpurohit et al. 2013) assuming a temperature of 2500 K, surface gravity of $10^3 \, \mathrm{m\,s^{-2}}$, and metallicity of 0 dex, as in Turbet et al. (2018). For planets orbiting an ultracool star like TRAPPIST-1, the bolometric albedo of water ice and snow is significantly lowered (Joshi & Haberle 2012; Shields et al. 2013; von Paris et al. 2013) due to the shape of its reflectance spectrum, as explained in Warren & Wiscombe (1980) and Warren (1984). To account for this effect, LMD-G computes the wavelength-dependent albedo of water ice and snow following a simplified albedo spectral law, previously calibrated to match the ice and snow bolometric albedo of 0.55 around a Sun-like star (Turbet et al. 2016). Around TRAPPIST-1, the average bolometric albedo for water ice and snow has been estimated to be $\sim$0.21 (Turbet et al. 2018).

Table 1
Parameters for the TRAPPIST-1 Planets in the HZ

Parameters	TRAPPIST-1e	TRAPPIST-1f	TRAPPIST-1g
Period (days)	6.10	9.21	12.35
Transit duration (s)	3433	3756	4104
F_p ($S_\oplus$)	0.662	0.382	0.258
Mass ($M_\oplus$)	0.772	0.934	1.148
Gravity ($g_\oplus$)	0.930	0.853	0.871
Radius ($R_\oplus$)	0.910	1.046	1.148
Visibility (transits)	85	55	42

Note. Here $S_\oplus$, $M_\oplus$, $g_\oplus$, and $R_\oplus$ correspond to Earth's insolation, mass, gravity, and radius, respectively. The visibility corresponds to the maximum number of times the planets' transit will be observable during *JWST*'s 5 yr nominal lifetime.

2.1.2. Microphysics

For each of the simulations performed in this study, water vapor was treated as a variable species. In other words, the relative water vapor humidity is set free, and supersaturation is not permitted by the LMD-G moist convective adjustment scheme (Leconte et al. 2013b). Water phase transitions, such as melting, freezing, condensation, evaporation, and sublimation, as well as water precipitation, were also considered. Water precipitation was computed with the scheme of Boucher et al. (1995). Similarly, the possible condensation and/or sublimation of CO_2 in the atmosphere (and on the surface) has been taken into account, but not the radiative effect of CO_2 ice clouds, because their scattering greenhouse effects (Forget & Pierrehumbert 1997) are low around cool dwarf stars such as TRAPPIST-1 (Kitzmann 2017) and are also limited by partial cloud coverage (Forget et al. 2013). When/where H_2O and/or CO_2 condenses, evaporates, or sublimates, the effect of latent heat is also taken into account. The CO_2 and H_2O cloud particle sizes were estimated from the amount of condensed material and the number density of cloud condensation nuclei (CCNs). The CCNs have been set up to a constant value of 10^6 kg^{-1} for liquid water clouds, 10^4 kg^{-1} for water ice clouds (Leconte et al. 2013a), and 10^5 kg^{-1} for CO_2 ice clouds (Forget et al. 2013) everywhere in the atmosphere. Ice particles and liquid droplets were sedimented following a Stokes law from Rossow (1978).

2.1.3. Climate Simulations of TRAPPIST-1e, 1f, and 1g

In this work, we have performed GCM simulations of the TRAPPIST-1 planets using planetary properties from Gillon et al. (2017b) and Grimm et al. (2018). A summary of the planetary properties used in this work is provided in Table 1. We have considered here only the three planets located in the classical HZ (Kopparapu et al. 2013), namely TRAPPIST-1e, 1f, and 1g, which are all assumed to be fully covered by a 100 m deep ocean (aquaplanets with no orography) with a thermal inertia of 12,000 J m^{-2} K^{-1} s^{-2} with no OHT.

For such a close-in system, the planets are believed to be in synchronous rotation (Turbet et al. 2018). In a synchronous rotation regime, thermal inertia should only affect the variability of the atmosphere. The horizontal resolution adopted for all of the simulations is a 64×48 coordinate in longitude × latitude (e.g., $5°.6 \times 3°.8$). In the vertical direction, the atmosphere is discretized in 26 distinct layers (model top at 10^{-5} bars) using the hybrid σ coordinates, while the ocean is discretized in 18 layers. The dynamical, physical, and radiative transfer time steps have been set up to set to 90, 900, and 4500 s, respectively.

For each of the three planets, the atmospheric configurations below have been modeled. The motivation for their selection is to highlight the impact of the following aerosols: H_2O (liquid and ice), CO_2 ice, and photochemical organic hazes.

1. Modern Earth-like (1 bar of N_2, 376 ppm of CO_2): expected to form H_2O clouds.
2. Archean Earth-like:
   (a) Charnay et al. (2013) case A (0.998 bar of N_2, 900 ppm of CO_2, 900 ppm of CH_4): expected to form H_2O clouds and photochemical hazes (see Section 2.2).
   (b) Charnay et al. (2013) case B (0.988 bar of N_2, 10,000 ppm of CO_2, 2000 ppm of CH_4): expected to form H_2O clouds and photochemical hazes (see Section 2.2).
   (c) Charnay et al. (2013) case C (0.898 bar of N_2, 100,000 ppm of CO_2, 2000 ppm of CH_4): expected to form H_2O clouds.
3. CO_2-dominated atmospheres:
   (a) 1 bar surface pressure: expected to form H_2O and CO_2 clouds.
   (b) 10 bars surface pressure: expected to form H_2O and CO_2 clouds.

Each simulation was run until the radiative equilibrium had been reached at the top of the atmosphere (TOA), typically after a couple of tens of Earth years. Simulations that led to unstable CO_2 surface collapse, i.e., when the rate of CO_2 surface condensation reached a positive constant (Turbet et al. 2017b, 2018), were stopped. Note that the 1 and 10 bar pressures are estimated according to the planet's gravity. In our simulations, the integrated atmospheric mass column is scaled in g_0/g, with g the surface gravity of the planet and g_0 the surface gravity on Earth.

2.2. Simulation of the Photochemistry

Our 3D model does not compute photochemistry prognostically. Therefore, we use an off-line 1D photochemistry code (Atmos) in order to compute the prevalence of minor gas species and organic hazes. To extend that set of gas species, a photochemical model has to be used in order to accurately simulate the formation and destruction of photochemical species and, eventually, the formation of photochemical hazes. In this study, we used the Atmos 1D model for our modern and Archean Earth-like simulations (as neither sulfuric acid nor hydrocarbon hazes are expected to form in the CO_2-dominated atmospheres, given our environmental assumptions).

Atmos is a 1D radiative-convective climate model coupled with a 1D photochemistry model, originally developed by James Kasting's group, that has been used to determine the edges of the HZ, simulate an Archean Earth atmosphere, and study various exoplanets (Arney et al. 2016, 2017; Lincowski et al. 2018; Meadows et al. 2018). The 1D representation of the atmosphere is plane-parallel at hydrostatic equilibrium. The vertical transport takes into account molecular and eddy diffusion. Atmos includes molecules that have O, H, C, S, N, and Cl atoms. For the modern Earth-like simulation, 309 reactions between 74 species have been considered, while for the Archean Earth-like simulation, 459 reactions between 97 species have been used. Depending on the reaction, the JP-15

Table 2
Surface Boundary Conditions for the Modern and Archean Earth-like (Charnay et al. 2013; Case B) Simulations

Species	Modern Earth Boundary Conditions	Archean Earth (Charnay B) Boundary Conditions
N_2	$VMR_0 = 0.78$	$VMR_0 = 0.99$
O_2	$VMR_0 = 0.21$	$VMR_0 = 4 \times 10^{-8}$
CO_2	$VMR_0 = 4 \times 10^{-4}$	$VMR_0 = 1 \times 10^{-2}$
CH_4	$F = 6.8 \times 10^8$	$VMR_0 = 2 \times 10^{-3}$
O	$v = 1.0$	$v = 1.0$
H	$v = 1.0$	$v = 1.0$
OH	$v = 1.0$	$v = 1.0$
HO_2	$v = 1.0$	$v = 1.0$
H_2O_2	$v = 0.2$	$v = 1.0$
H_2	$v = 2.4 \times 10^{-4}$	$VMR_0 = 5.3 \times 10^{-7}$
CO	$v = 0.03, F = 3.7 \times 10^{11}$	$v = 1.2 \times 10^{-4}$
HCO	$v = 1.0$	$v = 1.0$
H_2CO	$v = 0.2$	$v = 0.2$
HNO	$v = 1.0$	$v = 1.0$
NO	$v = 1.6 \times 10^{-2}, F = 6.0 \times 10^8$	$v = 3.0 \times 10^{-2}, F = 1.0 \times 10^9$
NO_2	$v = 3.0 \times 10^{-3}$	$v = 3.0 \times 10^{-3}$
H_2S	$v = 0.02, F = 2.0 \times 10^8$	$VMR_0 = 5.0 \times 10^{-12}$
SO_2	$F = 9.0 \times 10^9$	$VMR_0 = 2.6 \times 10^{-10}$
H_2SO_4	$v = 1.0, F = 7.0 \times 10^8$	$v = 1.0$
HSO	$v = 1.0$	$v = 1.0$
OCS	$v = 0.01, F = 1.5 \times 10^7$	$v = 0.01$
HNO_3	$v = 0.2$	$v = 0.2$
N_2O	$v = 0.0$	$v = 0.0$
HO_2NO_2	$v = 0.2$	$v = 0.02$
CS_2	$F = 2.7 \times 10^7$	$VMR_0 = 3.0 \times 10^{-11}$
C_2H_6S	$F = 3.3 \times 10^9$	$F = 3.3 \times 10^9$

Note. Table derived from Lincowski et al. (2018). Here VMR_0 corresponds to a fixed volume mixing ratio at the surface, velocity depositions (v) are in units of cm s^{-1}, and fluxes (F) are in units of molecules cm^{-2} s^{-1}.

(Burkholder et al. 2015) or NIST 2005 (http://webbook.nist.gov/chemistry/fluid/) databases were used. The initial conditions, such as gas mixing ratios, outgassing fluxes, and/or surface deposition velocities, can be set at the top and bottom of the model. Table 2 shows the boundary conditions used for the modern and Archean Earth-like (from Charnay et al. 2013; case B) simulations. Boundary conditions from Lincowski et al. (2018) in Table 8 have been used for the modern Earth-like simulations, except for H_2O and cloud profiles, which have been provided from the LMD-G GCM outputs. For the Archean Earth-like simulation, CH_4 mixing ratios have been fixed at the value used in the GCM. The H_2, H_2S, SO_2, and CS_2 mixing ratios have also been fixed to help resolve convergence issues. Note that we have verified that fixing the mixing ratio of these species does not impact the transmission spectrum. In both the modern and Archean Earth-like simulations, the NO production from lightning in the troposphere is included at a rate of 1×10^9 molecules cm^{-2} s^{-1} (see NO flux in Table 2).

The radiative transfer routine of Atmos uses the correlated k-absorption coefficients (Lacis & Oinas 1991) derived from the HITRAN 2008 (Rothman et al. 2009) and HITEMP 2010 (Rothman et al. 2010) databases for pressures of 10^{-5}–10^2 bars and temperatures of 100–600 K. Photochemical haze (tholins) optical properties are derived from Khare et al. (1984) for the longwave and Gavilan et al. (2017) for the shortwave. The photochemically active wavelength range of the model has

recently been extended to include the Lyα for a large set of species (Lincowski et al. 2018).

In this study, the photochemistry calculations are restricted to the terminator (longitude $\pm 90°$) because it is the only region for which the atmosphere can be probed with transmission spectroscopy. Because photochemistry occurs on the substellar hemisphere, we assume here a solar zenith angle (SZA) of 60° and that the photochemical species are then transported toward the terminator by dynamics (Chen et al. 2018). Note that the formation of hazes at lower zenith angles would not necessarily increase the haze production rate because of the UV self-shielding by hazes (Arney et al. 2016, 2017). The transport of hazes from the dayside to the terminator, requiring a full coupling between the GCM and photochemical model, is outside the scope of this paper but will be investigated in future studies.

To simulate the photochemical evolution around the terminator, we feed Atmos the temperature/pressure profiles and mixing ratios from the LMD-G outputs for each latitude coordinate around the terminator. Because we use a 64 × 48 longitude × latitude grid, Atmos is run 48 times around the terminator. To link the LMD-G GCM to the Atmos photochemical model, we have interpolated temperature and pressure profiles from the top of the GCM grid (going to ~10^{-5} bars, i.e., about 65 km) to the top of the Atmos photochemical model grid (going up to ~0.05 Pa, i.e., about 100 km). The temperature at an altitude of 100 km has been arbitrarily set to 150 K, similar to the thermosphere temperature on Earth. The temperature from the GCM lid to 100 km is then linearly decreasing to mimic the decreasing temperature in Earth's mesosphere. We made the following assumptions for these simulations.

1. Atmos is not coupled to LMD-G; we only feed the mixing ratio and temperature/pressure profiles from LMD-G to Atmos and run the photochemical model.
2. No biomass fluxes are considered.
3. Mixing ratios from LMD-G have been kept constant from the top of the GCM grid up to the top of the Atmos grid.
4. The water profile modified by Atmos does not affect the cloud location and properties because the water photolysis appears in the upper atmosphere, beyond the upper limit of the GCM.
5. Pressure and temperature profiles are extrapolated from the top of the GCM grid up to the top of the Atmos grid. Pressure decreases exponentially, taking into account atmospheric scale height, and the temperature decreases linearly down to 150 K at 100 km.
6. The SZA is fixed at 60°, assuming that photochemical species at the terminator are produced and transported from the dayside (Chen et al. 2018).

Therefore, our methodology is not a "coupling," and there is no feedback from the photochemical model to the GCM. A full coupling between LMD-G and Atmos will be investigated in future work.

When the photochemical model has converged, the new mixing ratios are computed for the following gases: N_2, H_2O, CH_4, C_2H_6, CO_2, O_2, O_3, CO, H_2CO, HNO_3, NO_2, SO_2, N_2O, and H_2, with some gases being more relevant for either the modern or Archean Earth-like template. If aerosols (clouds and/or photochemical hazes) are formed, then atmospheric profiles of gas and aerosols are used to compute the transmittance with the Planetary Spectrum Generator (PSG)
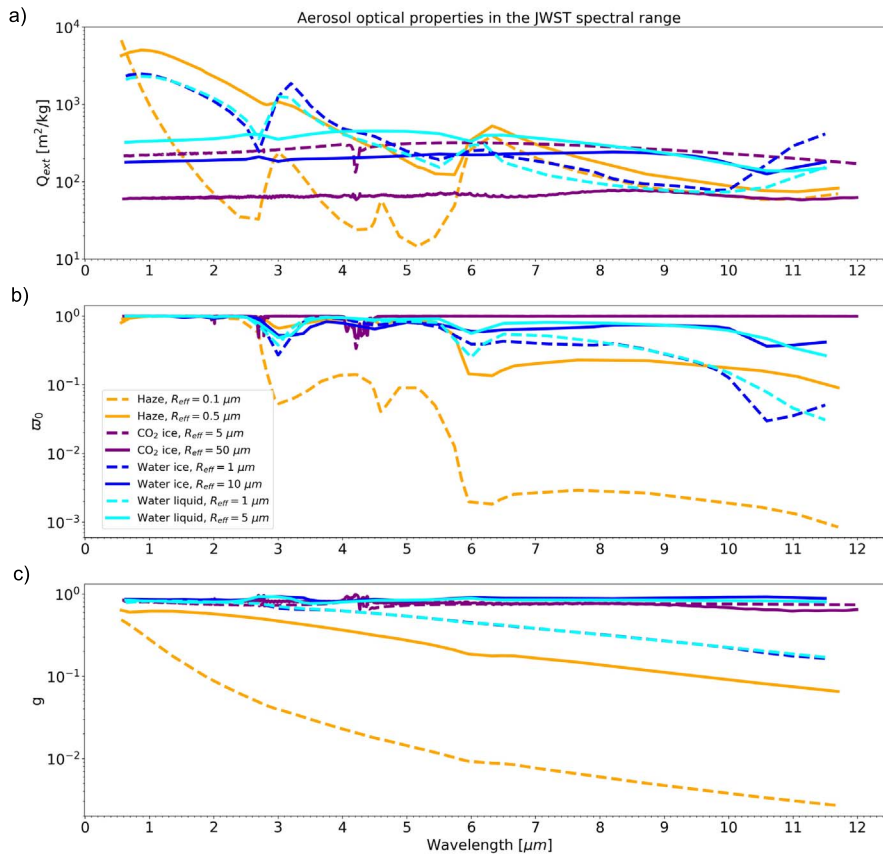
Figure 1. (a) Extinction cross section (Q_{ext}), (b) single scattering albedo (ϖ_0), and (c) asymmetry parameter of the phase function (g) as a function of the wavelength across the *JWST* NIRSpec Prism and MIRI LRS ranges.

through the terminator for each of the TRAPPIST-1 planets in the HZ and each of the atmospheric configurations.

2.3. Simulation of the Transmission Spectra

We use the PSG (Villanueva et al. 2018) to simulate *JWST* transmission spectra. The PSG is an online radiative transfer code for various objects of the solar system and beyond. It can compute planetary spectra (atmospheres and surfaces) for a wide range of wavelengths (UV/visible/near-IR/IR/far-IR/THz/submillimeter/radio) from any observatory, orbiter, or lander and also includes a noise calculator.

2.3.1. Aerosol Optical Properties

Four different kinds of aerosols are included in the simulated atmospheres: liquid and ice water, CO_2 ice, and fractal organic hazes. The optical properties of liquid and ice water, as well as the fractal organic hazes, are derived from HITRAN-RI 2016 from Massie & Hervig (2013), while the CO_2 ice cloud optical properties are obtained from Hansen et al. (1991).

Figure 1 shows the optical properties of the various aerosols formed by the LMD-G GCM (liquid water, ice water, and CO_2 ice) and the Atmos photochemical model (organic hazes). For each of them, the dashed line represents the smallest effective radius (R_{eff}), and the solid line denotes the largest R_{eff} formed in the atmosphere. The single scattering albedo (ϖ_0) shows that the smallest hazes are strongly absorbing (small ϖ_0) at most of the wavelengths, while the other aerosols produce a significant amount of scattering ($\varpi_0 \sim 1$) but progressively become more

absorbent in the infrared. Similarly, the asymmetry parameter of the scattering phase function (g) shows that the scattering of the smallest hazes is almost isotropic (small g indicating a Rayleigh regime), while the other aerosols have g values close to 1 (forward scattering), progressively decreasing in the infrared for the smallest (1 μm) liquid and ice water particles. Therefore, this figure shows that the type of aerosol and its particle size have very different optical properties, which will have different impacts on the transmission of light through the planet's atmosphere.

2.3.2. JWST Instruments and Noise

The *JWST* has an aperture size of 6.5 m from tip to tip of its segmented mirror, which is equivalent to a 5.64 m diameter disk that we use in the PSG. We estimate that the NIRSpec Prism is the most suitable instrument of *JWST* to characterize TRAPPIST-1 planets with transmission spectroscopy because it has relatively wide wavelength coverage, from 0.6 to 5.3 μm, for a resolving power (R) of 300, and TRAPPIST-1 should not reach the saturation of the detector. Note that a partial saturation (in the SED peaks) strategy or alternate readout mode (Batalha et al. 2018) can yield considerably better results in terms of fewer transits required to reach a desired S/N on gas detections (Batalha et al. 2018; Lustig-Yaeger et al. 2019).

In addition, some interesting gaseous features for the Earth-like atmospheres (Archean and modern), such as the methane (CH_4) and ozone (O_3) absorption lines, are also accessible in the *JWST* MIRI range. The mode supporting time series observation is the low-resolution spectroscopy (LRS; $R = 100$) with a
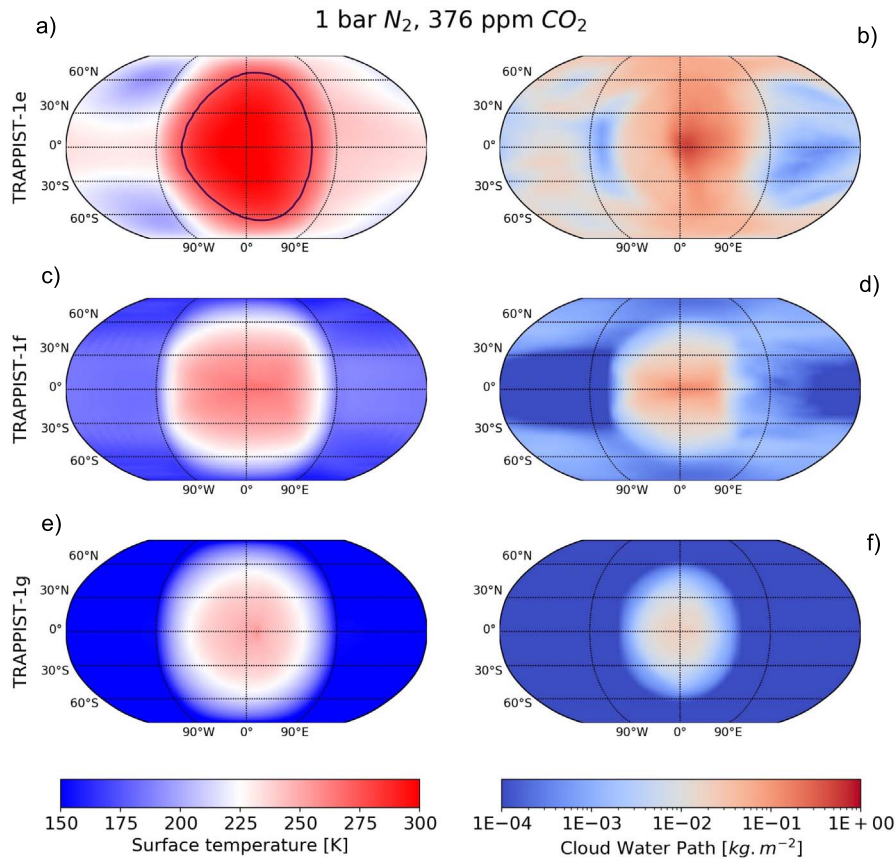
Figure 2. Surface temperature (left column) and cloud water path (right column) for TRAPPIST-1e (top row), 1f (middle row), and 1g (bottom row). The blue line shows the sea ice boundary. Note that only TRAPPIST-1e has any ice-free ocean.

wavelength range of 5.0–12.0 μm. In this work, spectra are shown with $R = 300$ across the NIRSpec and MIRI ranges to improve the visibility of the lines and have continuous spectra from 0.6 to 20 μm with a constant resolving power. However, to calculate the S/N in the MIRI range, we use $R = 100$ or below.

The PSG includes a noise calculator to account for the following: the noise introduced by the source itself (N_{source}); the background noise (N_{back}), following a Poisson distribution with fluctuations depending on $\sqrt{N}$, where N is the mean number of photons received (Zmuidzinas 2003); the noise of the detector (N_D); and the noise introduced by the telescope (N_{optics}). The total noise is then $N_{total} = \sqrt{N_{source} + N_{back} + N_D + N_{optics}}$.

3. Modern Earth-like Atmospheres

3.1. Climate

Because Earth is the only known inhabited planet and its habitability has been studied extensively, when the question of a planet's habitability arises, an atmosphere with boundary conditions based on the modern Earth as shown in Table 2 is always a key case to consider. With LMD-G, we have considered a 1 bar atmosphere composed of N_2 and 376 ppm of CO_2. While modern Earth consists of 78% of N_2 and 21% of O_2, both gases have similar impacts on a planet's climate, so we only take into account N_2 for the GCM simulations. We will consider O_2 and other minor gases in the photochemistry computation with Atmos. The surface temperature and water cloud path (kg m^{-2}) for TRAPPIST-1e, 1f, and 1g are shown in

Table 3
Surface Temperatures (TS) and Integrated Column of Condensed Species for the Modern Earth-like Atmosphere

Parameters	Planets		
	TRAPPIST-1e	TRAPPIST-1f	TRAPPIST-1g
TS mean (K)	244	197	168
TS min (K)	194	157	126
TS max (K)	304	266	256
H_2O liq.* (10^{-3} kg m^{-2})	1.3	0.0	0.0
H_2O ice* (10^{-3} kg m^{-2})	13.6	6.0×10^{-1}	1.3×10^{-2}
CO_2 ice* (10^{-3} kg m^{-2})	0.0	0.0	0.0

Note. Values with an asterisk are averaged around the terminator only.

Figure 2. TRAPPIST-1e is the only planet to have an ice-free surface around the substellar point and a thick cloud deck going up to the terminator (especially at high latitudes pushed by Rossby waves from the substellar point). Thick clouds ($>10^{-3}$ kg m^{-2}) are present in the east terminator of TRAPPIST-1f but not in TRAPPIST-1g. Table 3 lists the mean, maximum, and minimum surface temperature, as well as the integrated column of condensed species, for TRAPPIST-1e, 1f, and 1g. We can see that both the surface temperatures and amount of condensed species are much lower for the modern Earth-like atmosphere than for the CO_2-dominated atmosphere at 1 bar surface pressure (see Table 7). The mean surface temperature of TRAPPIST-1e (244 K) is in very good agreement with 3D climate simulations with the CAM4

GCM (Wolf 2017; 241 K) and LMD-G GCM (Turbet et al. 2018; 248 K; a 4 K difference arises due to the use of updated planetary parameters) but far from the 1D simulation of Lincowski et al. (2018; 279 and 282 K for the clear and cloudy simulations, respectively).

Figure 3 shows the vertically averaged horizontal distribution of the cloud effective radius R_{eff} and the vertical distribution at the terminator along with the mass mixing ratio (MMR) for TRAPPIST-1f in the four atmospheric scenarios considered in this study: modern Earth, Archean Earth, and 1 and 10 bar CO_2-dominated atmospheres. The largest R_{eff} are associated with the largest MMRs due to the coalescence processes. The atmosphere with boundary conditions based on the modern Earth (see Table 2) is the coldest of the four scenarios, and we can see that clouds are confined closer to the surface than in the other three scenarios and will therefore have a smaller impact on the transmission spectra. Also, CO_2 ice and hazes form at higher altitudes than H_2O clouds and with larger MMRs. Therefore, we expect a stronger impact from them on the spectra than H_2O clouds. As in Figure 2, we can see an asymmetry between the east and west sides of the substellar point, where most of the water clouds are advected toward the east terminator because of Kelvin waves introduced by the Coriolis force. Therefore, there are more clouds (larger MMR) and larger R_{eff} at the east terminator than the west terminator. Such a difference can be potentially detected with time-resolved observations of the ingress and egress (Line & Parmentier 2016), but this is outside the scope of this study. Discussions about the three other scenarios in Figure 3 will be presented in the corresponding sections.

To simulate more gases in the planet's atmosphere than the ones used in the GCM climate module (N_2, CO_2, CH_4, and H_2O), we run the Atmos photochemical model at the terminator (ignoring feedback on the climate) from atmospheric profiles (temperature, pressure, and mixing ratios) computed by LMD-G. Figure 4 shows a selection of averaged atmospheric profiles around the terminator for TRAPPIST-1e, 1f, and 1g obtained with Atmos, as well as the atmospheric profile ratios between TRAPPIST-1f and 1e and between TRAPPIST-1f and 1g. There is a significant amount of H_2O in the lower atmosphere of TRAPPIST-1e compared to TRAPPIST-1f, because TRAPPIST-1e is warmer; hence, more water is brought into the atmosphere from convection and evaporation on the dayside, which is then transported to the terminator. However, this trend is reversed in the upper atmosphere (above ~40 km), where H_2O in the TRAPPIST-1e atmosphere, closer to the star, is strongly photodissociated. We can also see that CH_4 is about 70 times more abundant in TRAPPIST-1f below 60 km, where the reaction $CH_4 + OH \rightarrow CH_3 + H_2O$ is 2 orders of magnitude faster in TRAPPIST-1e (the excess of OH being produced by the larger amount of H_2O from the reaction $H_2O + O_1D \rightarrow OH + OH$); it then increases by a few orders of magnitude near the TOA. Ozone responses are complex depending on UV availability and trace species like HOx and NOx (Grenfell et al. 2014; Harman et al. 2018). Concerning the N_2O, its reactivity does not seem significant in the lower atmosphere with no change in volume mixing ratio. Above ~60 km, the photodissociation of N_2O by ultraviolet B (UVB; Segura et al. 2003; Grenfell et al. 2014) becomes important, reducing its relative proportion in TRAPPIST-1e. Finally, O_2 does not appear to be too different between TRAPPIST-1e and 1f, except in the upper atmosphere (⩾90 km), where O_2 is more

photolyzed for TRAPPIST-1e, closer to the star. Between TRAPPIST-1f and 1g, 1f receives more flux from TRAPPIST-1 and has a wetter atmosphere, leading to less CH_4, O_3, and N_2O overall but more NO_2. But, near the TOA, both O_2 and O_3 build up easier for TRAPPIST-1f because more H_2O is photodissociated, leading to more free oxygen. The atmospheric profiles presented here are then used, along with cloud profiles from LMD-G, to simulate the transmission spectra.

3.2. JWST Simulated Spectra: Impact of H_2O Clouds

The NIRSpec Prism and MIRI transmission spectra at $R = 300$ for TRAPPIST-1e, 1f, and 1g with the boundary conditions based on the modern Earth are presented in Figure 5. The relative transit depth, the S/N for one transit (S/N-1), and the number of transits needed to achieve 3σ and 5σ detections are summarized in Table 4 for selected absorption lines. A resolving power of $R = 30$ has been adopted to optimize the S/N (Morley et al. 2017) while determining the number of transits.

The mathematical expression between the relative transit depth and the transit atmospheric thickness is (Winn 2010)

$$\delta\Delta = (\delta R/R_s)^2 + (2 \times R_p \times \delta R)/R_s^2 \sim (2 \times R_p \times \delta R)/R_s^2 \tag{1}$$

with Δ and $\delta\Delta$ the transit depth and relative transit depth, respectively, in ppm; R_p the planet's radius; δR the transit atmospheric thickness; and R_s the radius of the star in kilometers. Note that $(R_p/R_s)^2$ represents the transit depth for an airless planet. We can see that $\delta\Delta$ is dependent on the planet's radius. The planetary radius is increasing from TRAPPIST-1e to 1f and 1g (see Table 1), leading to the largest transit depth for TRAPPIST-1g. Note that $\delta\Delta$ and δR decrease with decreasing temperature or increasing gravity. Yet TRAPPIST-1g is the coldest planet but also the one with the lowest gravity. Furthermore, the atmospheric refraction increases with the planet's distance to the host star, leading to an increase in the altitude of the continuum and therefore a reduction of the relative transit depth of the lines. Finally, Table 1 also reports the number of times the planets will transit in front of TRAPPIST-1 when in the visibility zone of JWST during its nominal lifetime of 5 yr. This number is reduced as the orbital period increases (85, 55, and 42 transits for TRAPPIST-1e, 1f, and 1g, respectively).

We can see in Figure 5 for TRAPPIST-1e that H_2O clouds raise the continuum level up to a few kilometers above the surface, flattening the H_2O lines and reducing the relative transit depth (or atmospheric thickness) of other species. TRAPPIST-1f and 1g are much less affected by clouds because the weakest convection farther away from the star mutes the cloud formation. We have determined that the H_2O line at 1.14 μm is the strongest H_2O line not being blended by CO_2 for such an atmosphere. Indeed, even the well-known 2.7 μm H_2O line is completely dominated by CO_2 in this same spectral region, because H_2O is confined to the lower atmosphere, where the opacity to the infrared radiation is high and the clouds are located. However, the relative transit depth of that H_2O line, or any other, is so low (only a few ppm) that it is very challenging to detect.

In the bottom panel of Figure 5, we can see that the differences between the planets are largest between TRAPPIST-1e and 1f
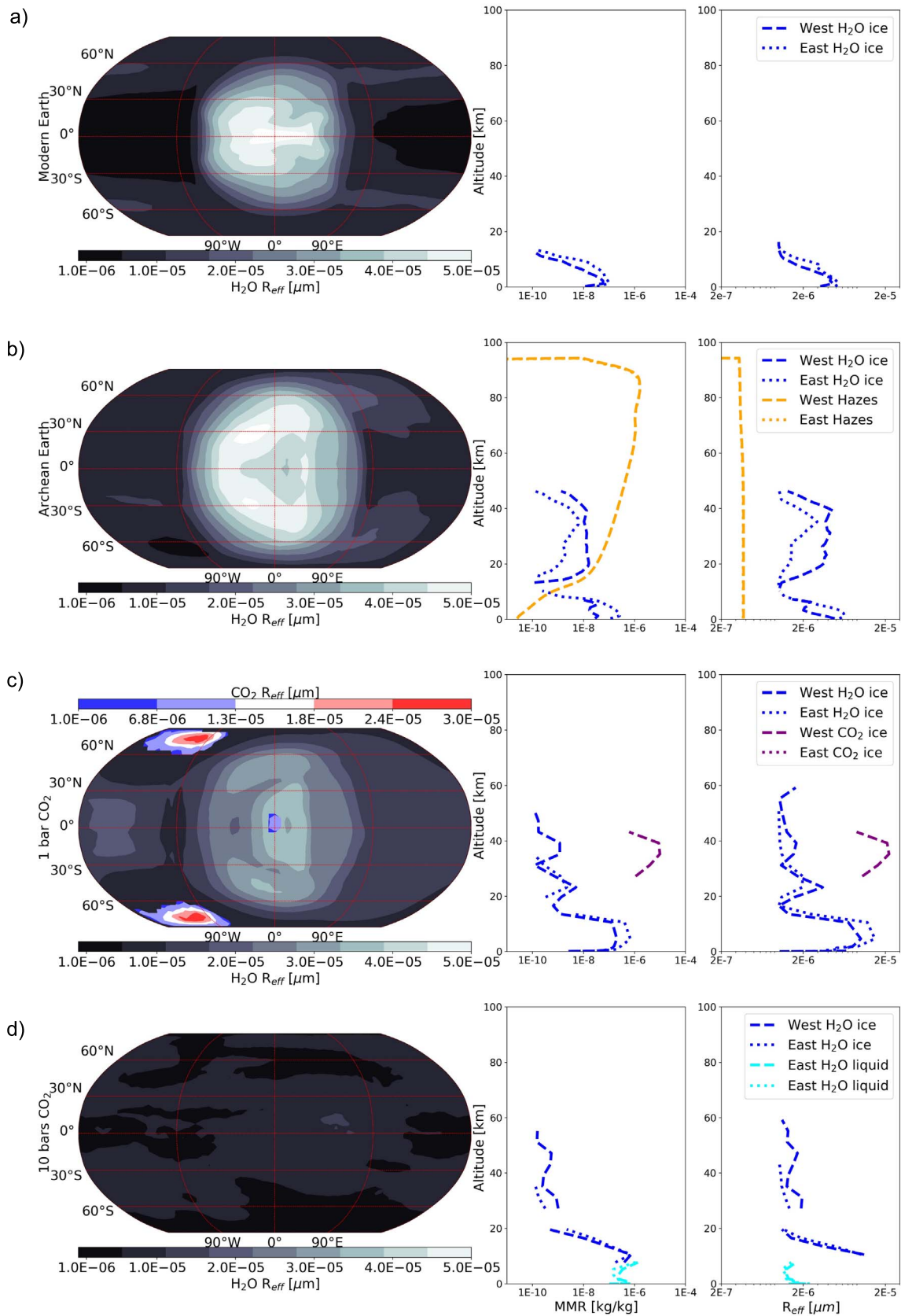
Figure 3. Left panels: vertically averaged cloud effective radius (R_{eff}). Right panels: vertical distribution of the MMR and R_{eff} at the east and west terminator for various aerosols in the TRAPPIST-1f atmosphere. Note that hazes are only generated with the Atmos photochemical model. When the MMR is very low, typically below 10^{-10} kg/kg, the R_{eff} is tiny, and its dimensions and optical properties are poorly constrained. Therefore, LMD-G set up the $R_{\text{eff}} = 10^{-6}$ μm threshold as the minimum value to be output. Therefore, MMR values below 10^{-10} kg/kg and $R_{\text{eff}} \leqslant 10^{-6}$ μm have been excluded from the averaging.
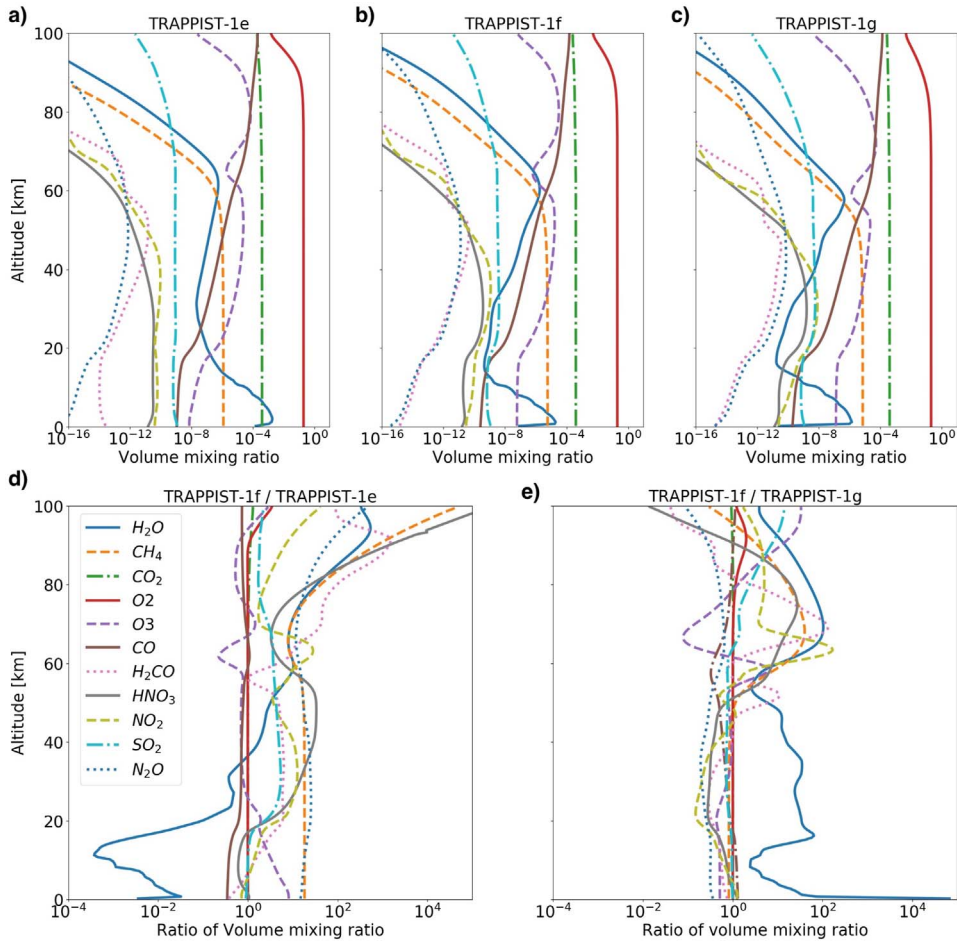
Figure 4. Gas mixing ratio profiles for atmospheres with boundary conditions based on the modern Earth (see Table 2) for (a) TRAPPIST-1e, (b) 1f, and (c) 1g, as well as profile ratios between (d) TRAPPIST-1f and 1e and (e) TRAPPIST-1f and 1g.

(solid lines), transiting from a wet and cloudy atmosphere to a drier and mostly cloud-free atmosphere. The largest difference between the clear-sky spectra concerns CH_4, which is strongly muted in TRAPPIST-1e, where it is destroyed by OH produced by the large amount of H_2O. TRAPPIST-1f and 1g are similar, with both in a snowball state (see Figure 2), and the difference between their transmission spectra (dashed lines) is small. In the NIRSpec Prism range, only CO_2 at 4.3 μm is detectable at 5σ during *JWST*'s nominal lifetime (TRAPPIST-1e, 1f, and 1g transiting 85, 55, and 42 times, respectively). Note that 35 and 21 transits are required to detect CO_2 at 5σ for the cloudy and clear-sky TRAPPIST-1e, respectively. These results are in relatively good agreement with Lustig-Yaeger et al.'s (2019) transit values obtained with NIRSpec Prism. The CH_4 at 3.3 μm could be detectable for TRAPPIST-1f and 1g at 3σ, but the transit depth of about 25 ppm could be below the noise floor (see Section 6). In the MIRI range, while some features, like O_3 at 9.6 μm, offer transit depths of the order of 40 ppm, the larger noise does not allow any detection at 3σ or 5σ in less than 100 transits.

4. Archean Earth-like Atmospheres

4.1. Climate

The climate of the Archean era (3.8–2.5 Ga) is still being debated. In this study, we chose to use the three Archean Earth atmospheric compositions by Charnay et al. (2013) that were previously simulated with LMD-G. Those configurations for a

1 bar surface pressure are dominated by N_2 with the following amount of greenhouse gas (GHG):

1. Charnay case A (900 ppm of CO_2, 900 ppm of CH_4),
2. Charnay case B (10,000 ppm of CO_2, 2000 ppm of CH_4), and
3. Charnay case C (100,000 ppm of CO_2, 2000 ppm of CH_4).

The surface temperatures and water cloud columns are displayed in Figures 6 and 7, respectively. Mean, minimum, and maximum values are reported in Table 5.

Again, we were not able to find a stable climate state for TRAPPIST-1g with a Charnay case C atmosphere, because CO_2 condenses on the nightside.

In Figure 6, we can see that the surface temperature is increasing from Charnay case A to Charnay case C for TRAPPIST-1e, while for TRAPPIST-1f and 1g, the surface temperature is maximum for Charnay case A, followed by case C, and finally case B. On the one hand, for TRAPPIST-1e, the atmosphere is warm and moist, and water feedback has a large effect, as well as the change of albedo due to clouds and the ratio of water/ice surfaces; on the other hand, for TRAPPIST-1f and 1g, the drier atmosphere leads to weak water feedback, and the increase of CH_4 from Charnay case A to Charnay case B promotes an anti-greenhouse effect more powerful than the increase of CO_2. As a result, Charnay case B is the coolest. In
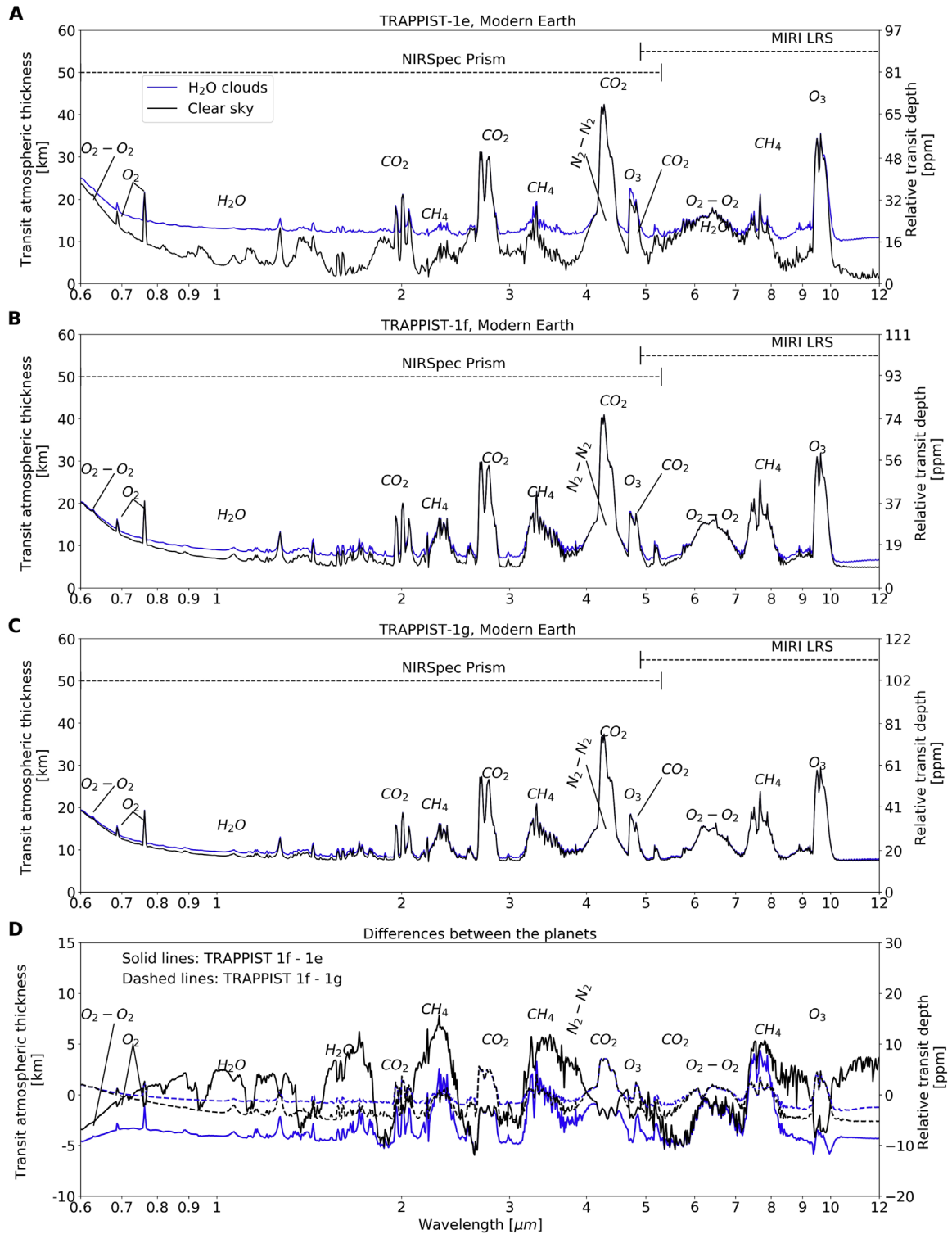
Figure 5. Simulated transmission spectra by *JWST* NIRSpec Prism and MIRI with $R = 300$ for aquaplanets (a) TRAPPIST-1e, (b) 1f, and (c) 1g with boundary conditions based on the modern Earth, as shown in Table 2. Panel (d) shows differences between planetary spectra.

Figure 7, the relative amount of condensed water between the cases follows the surface temperature, with the largest cloud coverage for TRAPPIST-1e being Charnay case C, while for TRAPPIST-1f and 1g, it is Charnay case A.

For planets for which the ratio of methane to carbon dioxide (CH_4/CO_2) in the atmosphere exceeds about 0.1, haze formation can occur (Arney et al. 2016). Such hydrocarbon haze is generated by methane photolysis from Lyα. Only

Charnay cases A and B have the required CH_4/CO_2 to produce photochemical hazes. For this study, we have performed the photochemistry and transmission spectra simulations only for Charnay case B. This case offers larger concentrations of CO_2 and CH_4 than Charnay case A and can produce photochemical hazes, contrary to Charnay case C. The Charnay case B Archean Earth-like atmospheric profiles are shown in Figure 8. In the Archean Earth-like GCM simulations, since fixed mixing

Table 4
Relative Transit Depth (ppm), S/N for One Transit (S/N-1), and Number of Transits to Achieve 5σ and 3σ Detection for Various Spectral Lines of the Modern Earth-like Atmosphere

Planets	TRAPPIST-1e	TRAPPIST-1f	TRAPPIST-1g
Instrument	NIRSpec Prism ($R = 30$)		
Feature	O_2 0.8 μm		
Depth (ppm)	5(10)	9(10)	10(11)
S/N-1	0.0(0.1)	0.1(0.1)	0.1(0.1)
No. of transits (5σ)	–	–	–
No. of transits (3σ)	–	–	–
Feature	H_2O 1.4 μm		
Depth (ppm)	2(10)	2(3)	3(3)
S/N-1	0.0(0.2)	0.1(0.1)	0.1(0.1)
No. of transits (5σ)	–	–	–
No. of transits (3σ)	–	–	–
Feature	CH_4 3.3 μm		
Depth (ppm)	12(20)	24(27)	25(26)
S/N-1	0.2(0.5)	0.5(0.6)	0.5(0.7)
No. of transits (5σ)	–	–(76*)	83*(74*)
No. of transits (3σ)	–(55)	36(27)	30(27)
Feature	CO_2 4.3 μm		
Depth (ppm)	47(61)	60(63)	58(60)
S/N-1	0.8(1.1)	1.1(1.2)	1.2(1.2)
No. of transits (5σ)	35(21)	20(18)	19(18)
No. of transits (3σ)	13(8)	7(6)	7(6)
Instrument	MIRI MRS ($R = 30$)		
Feature	O_2–O_2 6.5 μm		
Depth (ppm)	14(27)	22(26)	23(25)
S/N-1	0.1(0.2)	0.2(0.2)	0.2(0.2)
No. of transits (5σ)	–	–	–
No. of transits (3σ)	–	–	–
Feature	CH_4 7.7 μm		
Depth (ppm)	13(24)	29(33)	31(32)
S/N-1	0.1(0.2)	0.2(0.2)	0.2(0.2)
No. of transits (5σ)	–	–	–
No. of transits (3σ)	–	–	–
Feature	O_3 9.6 μm		
Depth (ppm)	36(48)	43(47)	44(46)
S/N-1	0.1(0.2)	0.2(0.3)	0.2(0.4)
No. of transits (5σ)	–	–	–
No. of transits (3σ)	–	–	–

Note. Numbers in parentheses are for clear sky only, while numbers without parentheses are the real values accounting for the impact of clouds. The hyphen represents the cases for which more than 100 integrated transits are needed, and asterisks denote the values above the maximum number of transits per planet during the *JWST* nominal lifetime mentioned in Table 1.

ratios of CO_2, CH_4, and N_2 are used, they are also constants for the photochemistry simulations with Atmos, along with other gases, such as O_2, H_2, H_2S, SO_2, and C_2H_6S. These fixed boundary conditions lead to no major differences in the lower atmosphere between the TRAPPIST-1e, 1f, and 1g profiles. However, TRAPPIST-1e receives more UV flux than TRAPPIST-1f, leading to more oxygen radicals from CO, CO_2, H_2O, etc. photodissociation (see the strong decrease of the gas profiles at the TOA). We can see in the TRAPPIST-1f/ TRAPPIST-1e subplot that much more O_2 and O_3 is produced

for TRAPPIST-1e above 20 km. Oxygen radicals consume the haze in TRAPPIST-1e, while for 1f, fewer hazes are consumed and their concentration is larger. Underneath the TRAPPIST-1f thicker haze layer (from 85 km), O_3 and NO_2 are protected from photodissociation by the haze shielding. On the other side, TRAPPIST-1g is farther away and has less UV flux, hence fewer hazes. Therefore, TRAPPIST-1f is at a sweet spot to maximize haze production, which shields O_3 and NO_2 from photodissociation. This thicker haze layer for TRAPPIST-1f will also have a dramatic impact on the transmission spectra (see Section 4.2).

4.2. *JWST Simulated Spectra: Impact of H_2O Clouds and Photochemical Hazes*

Figure 9 shows the TRAPPIST-1e, 1f, and 1g transmission spectra, and their relative differences, for a Charnay case B Archean Earth atmosphere with *JWST* NIRspec Prism and MIRI LRS. The hazes have a huge opacity down to the visible/ near-IR, which flattens most of the spectral features in the NIRSpec Prism range. In the relative difference subplot, we can see that hazes are responsible for most of the differences between the spectra, with the TRAPPIST-1f spectrum being up to 15 km (or ~30 ppm) higher, as explained in the previous section. We can also see in Figure 3(b) that the combination of the haze and H_2O ice clouds covers the whole atmospheric column for TRAPPIST-1f and therefore strongly absorbs the transmitted light.

In the MIRI range, the hazes are clearly visible between 6 and 7 μm, but at higher wavelengths, their opacity progressively decreases (see Figure 1), and clouds become the largest source of opacity in the spectrum for TRAPPIST-1e and 1g (haze opacity in TRAPPIST-1f dominates the cloud opacity across the whole wavelength range). Similar to Figure 5, clouds make a difference between the large cloud coverage of TRAPPIST-1e and the small cloud coverage of 1f and 1g. The combined impact of clouds and hazes in the detectability of gaseous features is summarized in Table 6. TRAPPIST-1g is the coldest and most distant of the three planets. Less starlight heats the substellar point, muting the convection and therefore producing fewer clouds. Also, farther away from the star, fewer UV photons are available to photodissociate CH_4 and form hazes. Therefore, TRAPPIST-1g has the smallest amount of clouds and hazes, allowing for fewer transits to detect the spectral lines than for the two other planets, but fewer transits are available during the *JWST* lifetime (see Table 1). The most favorable band to detect such atmospheres is CO_2 at 4.3 μm, despite the presence of hazes at this wavelength, with only about 23, 14, and 9 transits required for a 5σ detection. The strength of the nearby CO feature is too weak to be detectable because of the continuum raised by hazes but also because, as mentioned previously, CO abundances may have been underestimated by fixing the modern Earth mixing ratio and not predicting CO fluxes. The CH_4 at 7.7 μm is only detectable with MIRI at 3σ for TRAPPIST-1f and 1g (52 and 35 transits, respectively), while it will not be detectable at all with NIRSpec Prism at 1.2 μm because of the presence of hazes. The H_2O lines are either too shallow or blended by CH_4 or CO_2 so that they are undetectable.
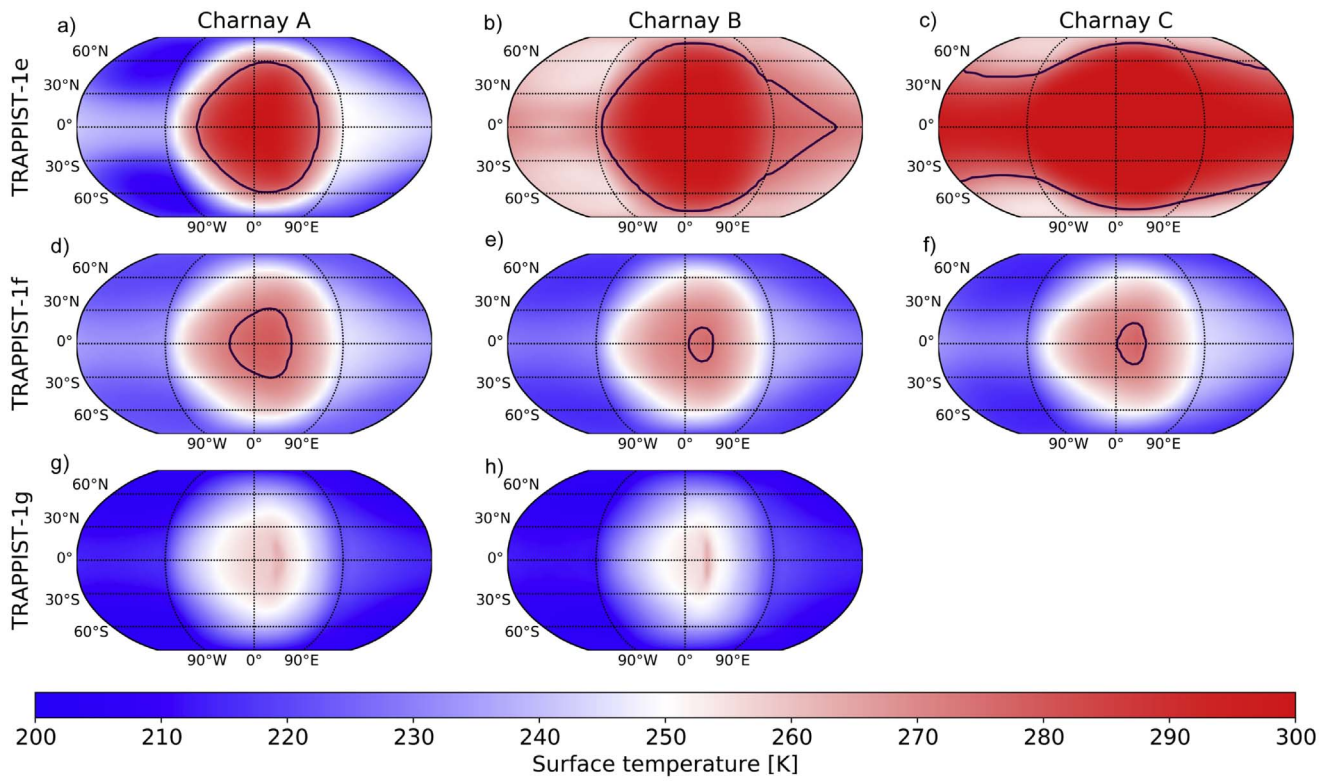
Figure 6. Surface temperature map in K for aquaplanets TRAPPIST-1e (top row), 1f (middle row), and 1g (bottom row) for Charnay et al. (2013) case A (left), B (middle), and C (right) Archean Earth atmospheres. TRAPPIST-1g case C is missing because the CO_2 in the atmosphere has condensed to the nightside, leading to the crash of the simulation. The blue line shows the sea ice boundary.
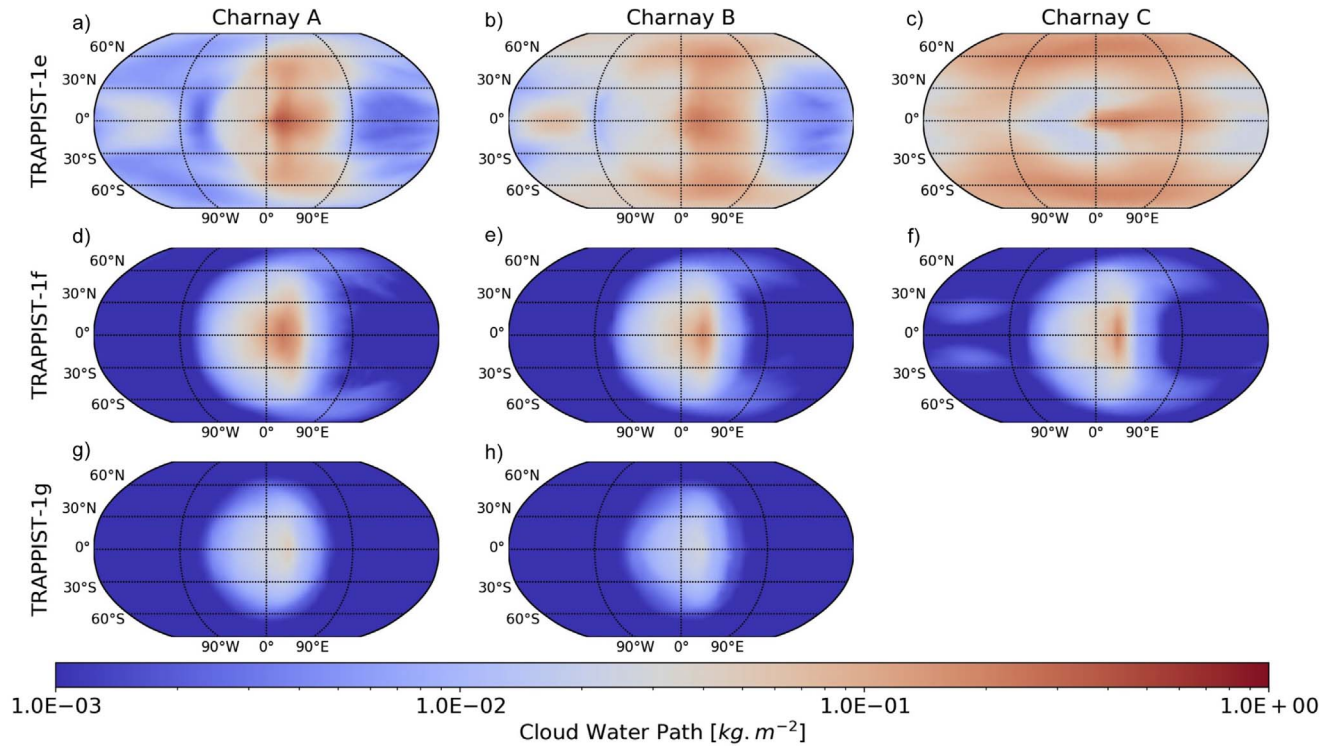
Figure 7. Integrated cloud water column in kg m^{-2} for aquaplanets TRAPPIST-1e (top row), 1f (middle row), and 1g (bottom row) for Charnay et al. (2013) case A (left), B (middle), and C (right) Archean Earth atmospheres. TRAPPIST-1g case C is missing because the CO_2 in the atmosphere has condensed to the nightside, leading to the crash of the simulation.
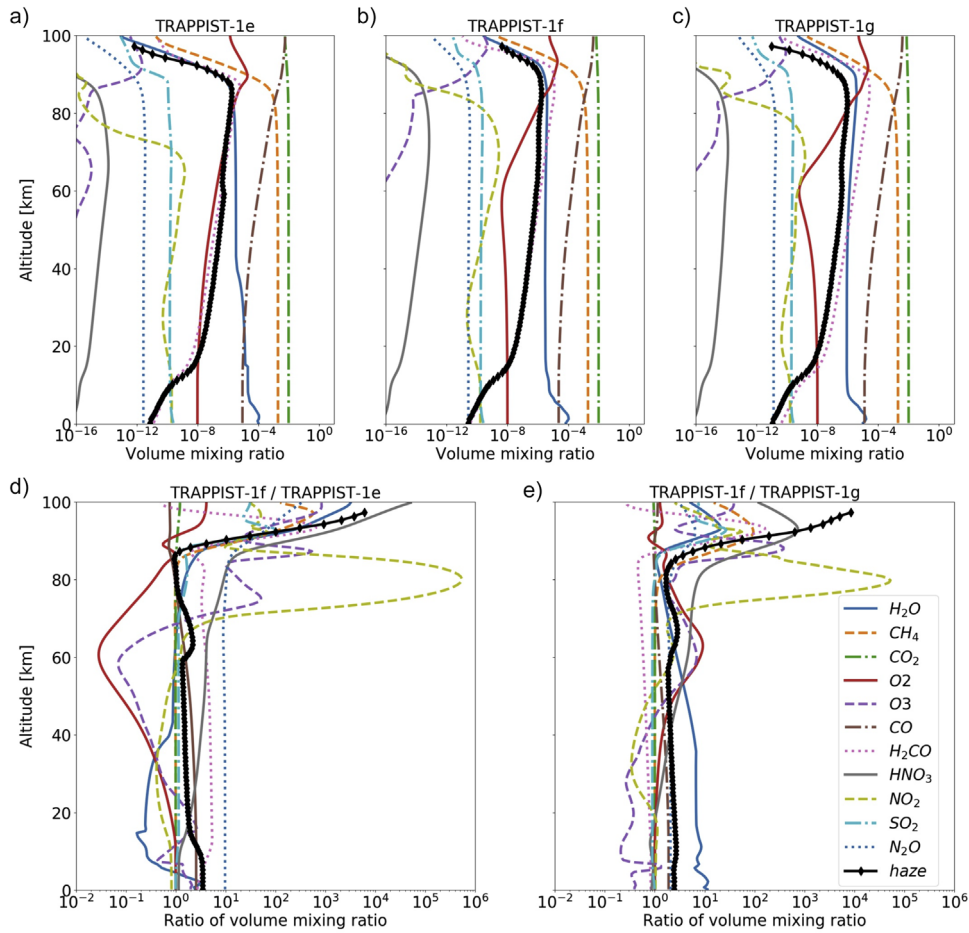
Figure 8. Gas mixing ratio profiles for an Archean Earth-like composition of Charnay et al. (2013) case B for (a) TRAPPIST-1e, (b) 1f, and (c) 1g, as well as profile ratios between (d) TRAPPIST-1f and 1e and (e) TRAPPIST-1f and 1g.

Table 5
Surface Temperatures (TS) and Integrated Column of Condensed Species for the Archean Earth-like Atmosphere

Parameters	Planets							
	TRAPPIST-1e			TRAPPIST-1f			TRAPPIST-1g	
Case	A	B	C	A	B	C	A	B
TS mean (K)	243	273	286	238	234	235	204	221
TS min (K)	207	254	254	219	215	214	203	205
TS max (K)	305	310	324	279	277	278	204	264
H_2O liq.* (10^{-3} kg m^{-2})	3.7	12.0	74.5	0.0	0.0	0.0	0.0	0.0
H_2O ice* (10^{-3} kg m^{-2})	12.6	24.7	26.1	1.1	0.81	0.93	0.07	0.05

Note. Values with an asterisk are averaged around the terminator only.

5. CO$_2$ Atmospheres

5.1. Climate

Among the four rocky planets of our solar system, CO$_2$ is the dominant gas on two of them (Venus and Mars) and is thought to have been a dominant gas in early Earth's atmosphere, in particular during the Hadean epoch (Zahnle & Schaefer 2010). Therefore, it is reasonable to think that CO$_2$ atmospheres may be common in other planetary systems as well. De Wit et al. (2018) and Moran et al. (2018) showed that if the TRAPPIST-1 planets have an atmosphere, they should be free of low mean molecular weight gases such as hydrogen or helium in the

absence of haze. This raises a possibility of high mean molecular weight species, such as CO$_2$, as a possible constituent. For each planet in the HZ of TRAPPIST-1 (i.e., planets e, f, and g), we used LMD-G to simulate CO$_2$-dominated atmospheres with 1 and 10 bar surface pressures. However, we were not able to successfully simulate the 1 bar CO$_2$ atmosphere for TRAPPIST-1g, because the atmospheric temperature on the nightside is cold enough that CO$_2$ condenses (below 194 K at 1 bar) on the surface, resulting in atmospheric collapse. TRAPPIST-1g retaining 1 bar or less of CO$_2$ is therefore highly unstable and unlikely to occur, as also found in Turbet et al. (2018). Figure 10 shows the surface temperature maps, averaged over 10 orbits, of 1 bar (left column) and 10 bars
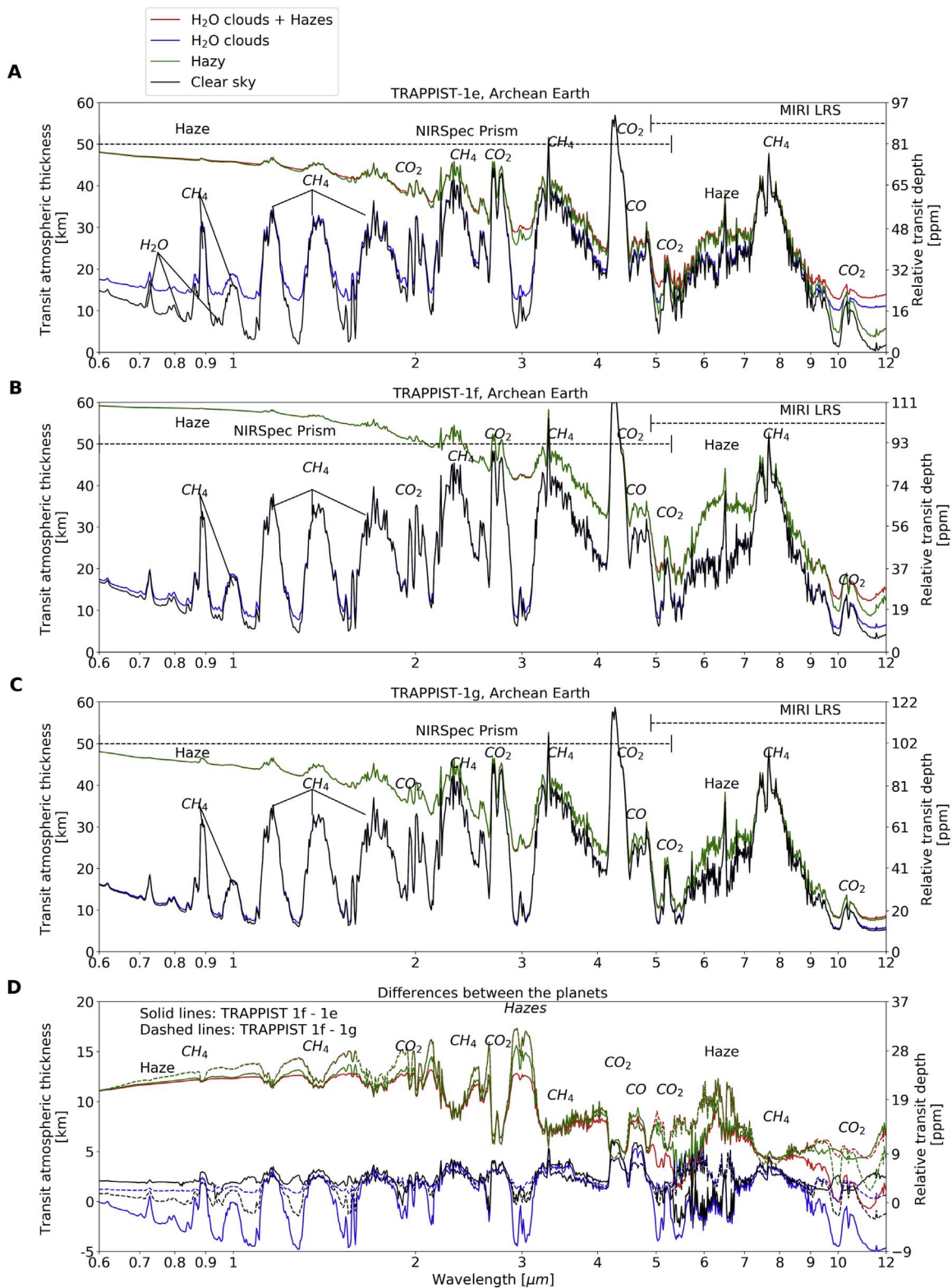
Figure 9. Simulated transmission spectra by *JWST* NIRSpec Prism and MIRI with $R = 300$ for aquaplanets (a) TRAPPIST-1e, (b) 1f, and (c) 1g with the Archean Earth atmosphere composition of Charnay et al. (2013) case B. Panel (d) shows differences between planetary spectra.

(right column) CO_2-dominated atmospheres for TRAPPIST-1e (top row), 1f (middle row), and 1g (bottom row). Surface temperatures and integrated columns of condensed species are reported in Table 7. As for the modern Earth-like atmosphere, mean surface temperatures predicted by the GCM for the 10 bar cases agree with other GCM simulations (Wolf 2017) but are much higher than the one predicted with the 1D climate model of Lincowski et al. (2018) for their 10 bar Venus-like atmospheres, primarily due to the cooling of the highly reflective sulfuric acid aerosols (not included in Wolf 2017 or our study). Note that none of the 10 bar simulations are cold enough to have CO_2 condensation at the surface (below 233.6 K), in agreement with Turbet et al. (2018). At

Table 6
Relative Transit Depth (ppm), S/N for One Transit (S/N-1), and Number of Transits to Achieve a 5σ and 3σ Detection for Various Spectral Lines of the Archean Earth-like Atmosphere of Charnay Case B

Planets	TRAPPIST-1e	TRAPPIST-1f	TRAPPIST-1g
Instrument	NIRSpec Prism ($R = 30$)		
Feature	CH$_4$ 1.2 μm		
Depth (ppm)	2(44)	1(55)	4(56)
S/N-1	0.1(1.0)	0.1(1.4)	0.1(1.5)
No. of transits (5σ)	−(23)	−(13)	−(12)
No. of transits (3σ)	−(8)	−(5)	−(4)
Feature	CO$_2$ 4.3 μm		
Depth (ppm)	59(85)	72(108)	86(111)
S/N-1	1.1(1.6)	1.4(2.2)	1.7(2.3)
No. of transits (5σ)	23(9)	14(5)	9(5)
No. of transits (3σ)	8(3)	5(2)	3(2)
Feature	CO 4.7 μm		
Depth (ppm)	4(39)	8(54)	8(53)
S/N-1	0.1(0.7)	0.1(1.0)	0.1(1.0)
No. of transits (5σ)	−(59)	−(27)	−(25)
No. of transits (3σ)	−(21)	−(10)	76*(9)
Instrument	MIRI MRS ($R = 30$)		
Feature	CH$_4$ 7.7 μm		
Depth (ppm)	44(66)	60(82)	67(86)
S/N-1	0.3(0.6)	0.4(0.8)	0.5(0.8)
No. of transits (5σ)	−(80)	−(44)	98*(36)
No. of transits (3σ)	−(29)	52(16)	35(13)

Note. Numbers in parentheses are for clear sky only, while numbers without parentheses are the real values accounting for the impact of clouds and hazes. The hyphen represents the cases for which more than 100 integrated transits are needed, and asterisks denote the values above the maximum number of transits per planet during the *JWST* nominal lifetime mentioned in Table 1.

1 bar, we can see that TRAPPIST-1e is ice-free, while TRAPPIST-1f is an "eyeball" planet, with an open ocean restricted to the substellar region, roughly between −40 and +40 longitude east and −40 and +40 latitude north. In both cases, the surface temperature contrast between the substellar and anti-substellar region is roughly 100 K. At 10 bars of surface pressure, the atmosphere is very efficient to transport the heat, and the contrast is only on the order of 10 K for TRAPPIST-1e, 1f, and 1g. Very interestingly, because of the faster rotation period of TRAPPIST-1e (6.1 days) a so-called "lobster pattern" appears, which is usually seen when a dynamic ocean is coupled to the atmosphere (Hu & Yang 2014; Del Genio et al. 2019). This asymmetric pattern of surface temperature is due to the combination of a Rossby wave west of the substellar point moving the warm air away from the equator and a Kelvin wave east of the substellar point progressing exclusively in the longitude–altitude plane. While OHT is not included in our simulation, the combination of the dense atmosphere and fast rotation rate are responsible for this pattern.

Figure 11 shows the integrated columns of H$_2$O condensates (liquid and ice). The largest cloud coverage was recorded for both TRAPPIST-1e and 1f at 1 bar, with a large cloud deck due to the strong convection and shifted eastward of the substellar point (Yang et al. 2014; Kopparapu et al. 2017) for TRAPPIST-1e due to the fast rotation. Note that for TRAPPIST-1f, the rotation is slower and the cloud deck is more centered toward the ice-free substellar region.
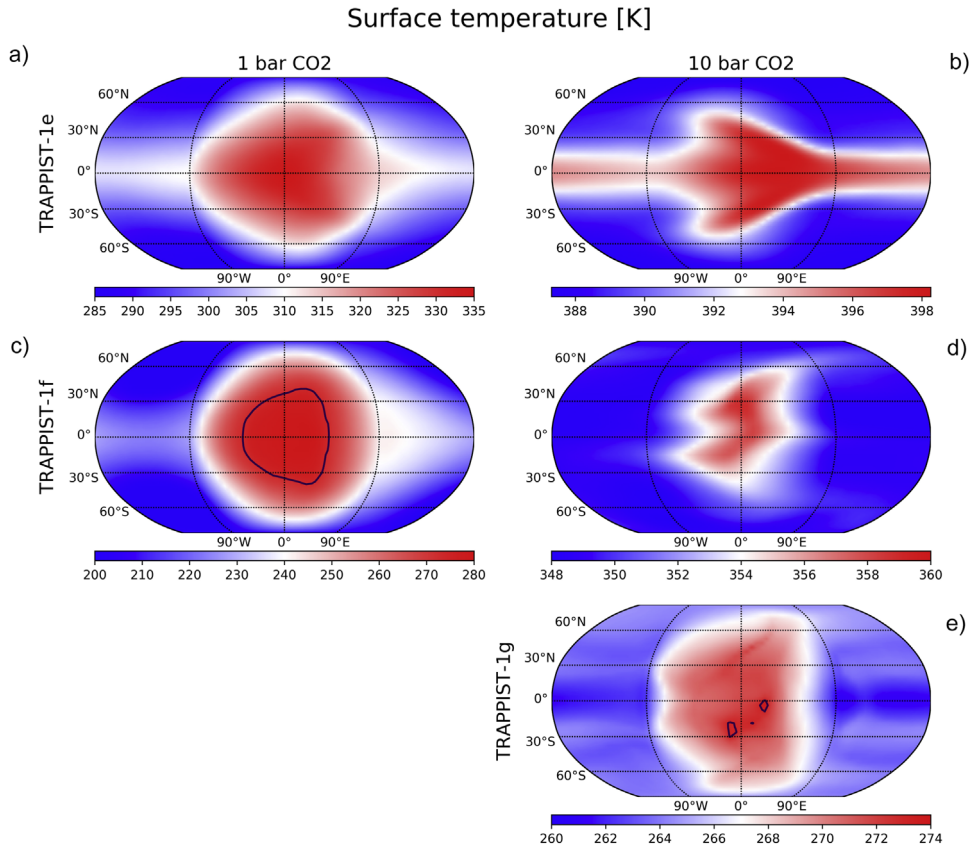
At 10 bars of surface pressure, TRAPPIST-1e and 1f are so warm that the huge amount of water vapor brought to the atmosphere leads to both inefficient radiative cooling and strong solar absorption in the low atmosphere, causing a net radiative heating of the layers near the surface; subsequently, this radiative heating creates a strong temperature inversion encompassing the entire planet, stabilizing the low atmosphere against convection, including at the substellar point (Wolf & Toon 2015). Indeed, inversion layers are intrinsically stable against vertical mixing; without a deep convection carrying moisture up from the boundary layer, no substellar cloud deck is formed. Instead, the skies are relatively clear despite the enormous amount of water vapor in the atmosphere. From the bottom panel of Figure 3, we can see that the TRAPPIST-1f atmosphere forms H$_2$O liquid clouds from zero to about 10 km and H$_2$O ice clouds from 10 to 60 km. Very thin CO$_2$ clouds also formed at high altitudes but are not shown in the figure. TRAPPIST-1g is much colder, almost fully ice-covered, except at a few spots near the substellar region (see Figure 10, bottom panel), where some water can evaporate from the ocean and form relatively thin clouds with an H$_2$O liquid cloud column of about 0.1 kg m^{-2}.

Figure 12 shows the integrated column of CO$_2$ ice. TRAPPIST-1e is too warm at 1 and 10 bars to have significant CO$_2$ condensation in the atmosphere. For TRAPPIST-1f, CO$_2$ starts to condense in two cold traps (Leconte et al. 2013b) at 1 bar at a symmetric position around longitude −120° and latitudes ±80° and between 30 and 50 km (see Figure 3), but their position can slightly vary due to planetary-scale equatorial Kelvin and Rossby wave interactions (Showman & Polvani 2011). Also, we notice that for a thicker atmosphere (10 bars), these two cold traps tend to move westward and toward the highest latitudes, and two others are at longitude +150° and latitudes ±90°. Note that a few spots of CO$_2$ condensate appear eastward of the substellar point for TRAPPIST-1e and at the substellar point for TRAPPIST-1f. This is due to a local temperature minimum at $p = 67$ mbar near the substellar point marking the top of the ascending circulation branch (Carone et al. 2014, 2015, 2018). These CO$_2$ clouds near the substellar point would likely disappear due to the shortwave absorption of the CO$_2$ ice crystals, but the radiative effect of CO$_2$ is not taken into account in our simulations.

5.2. JWST Simulated Spectra: Impact of H$_2$O and CO$_2$ Clouds

Figures 13 and 14 show *JWST* NIRSpec Prism and MIRI simulated transmission spectra for TRAPPIST-1e, 1f, and 1g at 1 and 10 bar CO$_2$ surface pressures, respectively. In addition, the relative difference between the transmission spectra for the 10 and 1 bar surface pressure atmospheres is shown in Figure 15 for TRAPPIST-1e and 1f. The relative transit depth, the S/N for 10 transits, and the number of transits for a 5σ and 3σ detection are reported in Table 8.

First, we can see in Figure 13 that water clouds produce a considerable flattening of the spectra of TRAPPIST-1e, suppressing H$_2$O lines and leading to a continuum level of about 22 km in the 1 bar case. Around the terminator, the average liquid and ice water contents (LWC and IWC, respectively) are equal to 4.1×10^{-6} and 6.5×10^{-7} kg m^{-3} for TRAPPIST-1e and 1f, respectively (see Table 7). The CO$_2$ clouds slightly raise the continuum in TRAPPIST-1f. The differences between the two spectra in the clear-sky atmosphere are due to the stronger H$_2$O lines in TRAPPIST-1e, while

Surface temperature [K]

Figure 10. Surface temperature map in K for aquaplanets TRAPPIST-1e (top row), TRAPPIST-1f (middle row), and TRAPPIST-1g (bottom row) at 1 (left column) and 10 (right column) bars of CO_2 surface pressure. TRAPPIST-1g at 1 bar is missing because the atmosphere would collapse on the nightside. Note that the temperature scale is different for each panel in order to highlight the so-called "lobster pattern" of TRAPPIST-1e at 10 bars, which has a thermal amplitude of only 10 K. The blue line shows the sea ice boundary. Note that TRAPPIST-1e at 1 and 10 bars is completely ice-free.

Table 7
Surface Temperatures (TS) and Integrated Column of Condensed Species for the CO_2-dominated Atmospheres

Planet	TRAPPIST-1e		TRAPPIST-1f		TRAPPIST-1g
	CO_2-dominated		CO_2-dominated		CO_2-dominated
Pressure	1 bar	10 bars	1 bar	10 bars	10 bars
TS mean (K)	303	392	230	350	266
TS min (K)	285	387	194	348	261
TS max (K)	335	398	281	359	274
H_2O liq.[*] (10^{-3} kg m^{-2})	61.3	28.3	1.0×10^{-2}	26.7	2.0×10^{-1}
H_2O ice[*] (10^{-3} kg m^{-2})	9.9	12.4	4.3	9.4	5.7
CO_2 ice[*] (10^{-3} kg m^{-2})	0.0	0.0	3.1×10^{-2}	6.6×10^{-1}	90.0

Note. Values with an asterisk are averaged around the terminator only.

the CO_2 lines are very similar. In the cloudy atmosphere, TRAPPIST-1e has the higher continuum and therefore the smaller absorption lines due to H_2O clouds.

Figure 14 shows a transition between TRAPPIST-1e to 1f and 1g, where the TRAPPIST-1 flux received by the planets is reduced. Lower fluxes imply colder surface temperatures leading to less water evaporation, lower water mixing ratios in the atmosphere, and shallower water lines. When less water vapor exists, fewer water clouds are produced, reducing the flattening of water lines and therefore paradoxically improving their detection. Indeed, we can see in Table 8 that the differences in transit depth between the clear-sky and cloudy

values are smallest for TRAPPIST-1g. TRAPPIST-1e is too warm to have CO_2 clouds to condense (see also Figure 12) but has an opaque H_2O cloud deck at about 28 km. TRAPPIST-1f has many fewer H_2O clouds, and a few CO_2 clouds slightly raise the continuum. Finally, the spectrum of the colder TRAPPIST-1g is the most impacted by CO_2 clouds, while the few H_2O clouds are below the atmospheric refraction limit (~15 km) and therefore not observable in the spectrum. In the relative difference subplot, we can see that the continuum and the H_2O lines are the major differences between the spectra of the three planets, while the intensities of the CO_2 lines are fairly similar.
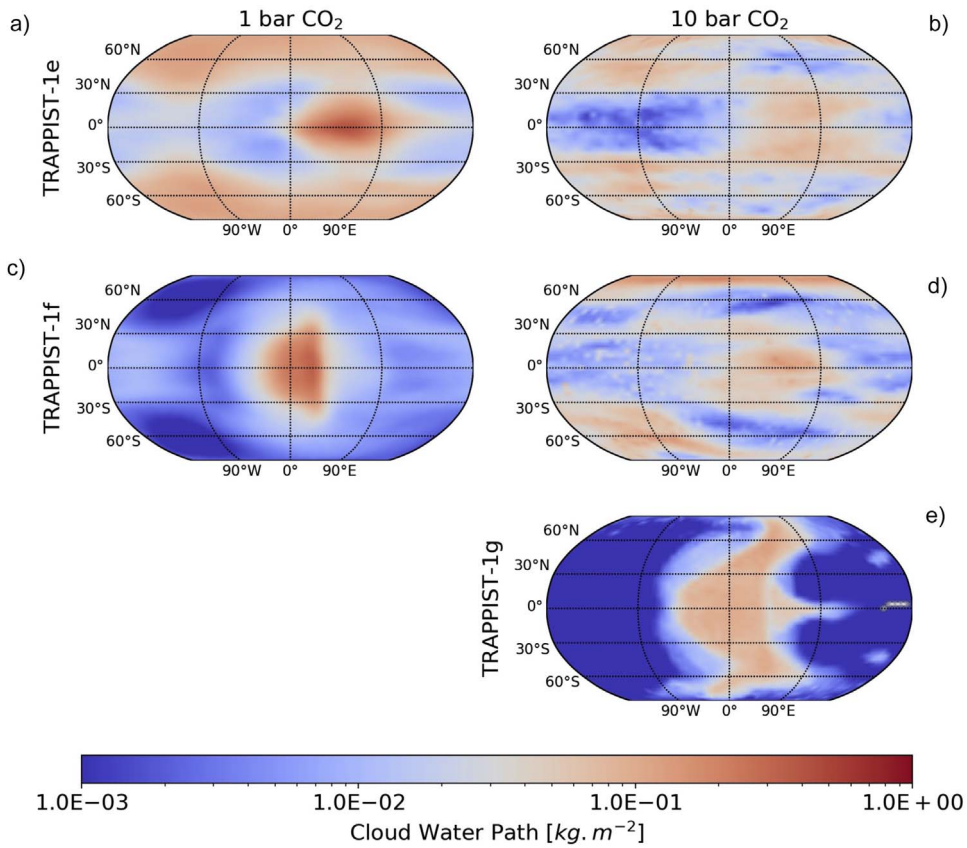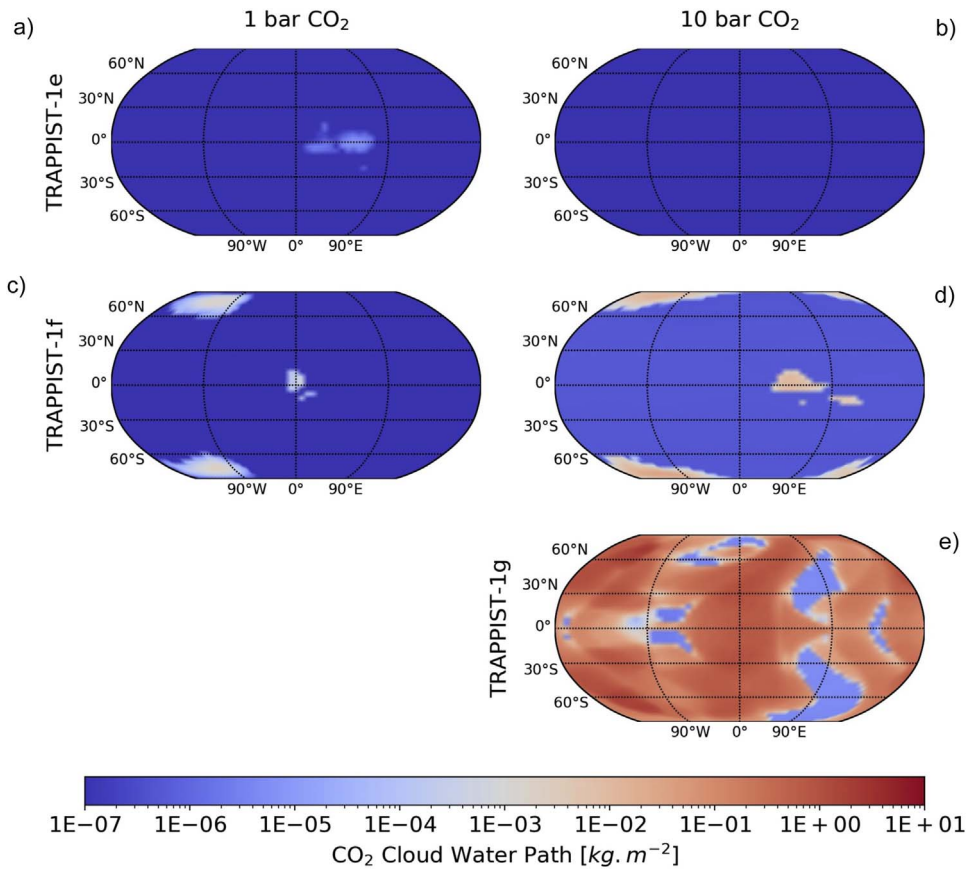
Figure 11. Integrated H_2O column in kg m^{-2} for aquaplanets TRAPPIST-1e (top row), TRAPPIST-1f (middle row), and TRAPPIST-1g (bottom row) at 1 (left column) and 10 (right column) bars of CO_2 surface pressure. TRAPPIST-1g at 1 bar is missing because the atmosphere has condensed to the nightside, leading to the crash of the simulation.

At 10 bars of surface pressure, the mean surface temperature of TRAPPIST-1e is very high, 392 K, compared to 303 K at 1 bar. At this temperature, the continuum of water vapor in the low atmosphere is opaque to the infrared radiation, and the continuum is pushed toward higher altitudes, even in clear sky, up to about 15 km. Figure 14 shows that this results in a reduction of the relative transit depth of every gas, including CO_2, compared with the spectra at 1 bar of surface pressure (Figure 13). This can also be seen in Figure 16, in units of atmospheric pressure, where clear-sky absorption lines are shallower at 10 bars than at 1 bar of surface pressure. This is counterintuitive because larger gas pressures are expected to produce stronger absorption lines, as long as the temperatures are assumed to be constant. However, as we can see in the bottom left plot of Figure 16, the temperature at the atmospheric pressures (10^5–10^3 Pa) where the lines are emitted (where the atmosphere goes from optically thick to optically thin) is colder at 10 bars than at 1 bar. Indeed, at 10 bars, the specific humidity of the atmosphere is much lower (bottom right plot), and the temperature lapse rate is getting steeper (closer to the dry adiabat; Wolf & Toon 2015), leading to a faster decrease of temperature. Yet the pressure-broadening half-width is inversely proportional to temperature. So, at the colder emission temperatures of the 10 bar atmospheres, the line broadens, and the peak intensity, relative to the continuum, becomes lower. However, because at 10 bars of surface pressure, the whole spectrum is raised toward higher altitudes,

it shows larger transit atmospheric thickness and transit depth relative to the ground than at 1 bar of surface pressure. As a result, Figure 15 shows the larger transit atmospheric thickness and transit depth at 10 bars in clear sky (more than 10 km or 15 ppm) for TRAPPIST-1e and 1f because of the continuum IR opacity, while the cloudy (H_2O) spectra show only a few kilometers of differences because clouds form roughly at the same altitude. Note that because we will not be able to differentiate a ground level from a cloud deck in this wavelength range with real observations, the overall result will be a reduction of the relative intensity of the absorption lines for the warmer 10 bar CO_2 surface pressure case.

Similar to the atmospheres with modern and Archean Earth boundary conditions, we can see that H_2O lines are not detectable at 3σ or 5σ in less than 100 transits for the cloudy scenario. MIRI does not perform better, with no detectable H_2O lines. On the contrary, the well-mixed CO_2 is barely affected by the presence of clouds in the line region, because enough of it remains above the cloud deck. Because the continuum level is raised by the presence of clouds, the transit atmospheric thickness and transit depth of CO_2 is also reduced. The CO_2 at 4.3 μm has a transit depth of the order of 50–80 ppm and could be detected with NIRSpec from 10 to 30 transits at a 5σ confidence level. Note that the number of transits at 5σ for the 10 bar clear-sky case of TRAPPIST-1e (22) is the same as the one estimated by Lustig-Yaeger et al. (2019) for the NIRSpec Prism sub512 mode.

Figure 12. Integrated CO_2 column in kg m^{-2} for aquaplanets TRAPPIST-1e (top row), TRAPPIST-1f (middle row), and TRAPPIST-1g (bottom row) at 1 (left column) and 10 (right column) bars of CO_2 surface pressure. TRAPPIST-1g at 1 bar is missing because the atmosphere has condensed to the nightside, leading to the crash of the simulation. All planets are aquaplanets.

## 6. Discussion

6.1. Noise and Detectability

In this section, we discuss the different noise sources that can impact *JWST* observations and the detectability of an atmosphere and/or any gaseous feature.

The large aperture of *JWST* (6.5 m) will allow us to quickly acquire a significant number of photons after a few transits, while the noise from the source (N_{source}) will largely dominate the total noise (N_{total}). In a photon-limited noise scenario, the noise can be represented by "white noise," which decreases when acquiring more photons. For transmission spectroscopy, it can be expressed by $1/\sqrt{X}$ or $X^{-0.5}$, where X is the number of transits. However, every instrument suffers from background red noise (of low frequency), which is a measurement error, in addition to the frequency coming from the white noise (photon, reading, dark, etc.). This red noise comes mainly from the systematic effects that affect the measurements, e.g., the fact that the pixels are not perfectly homogeneous (intrapixel gain variability; Knutson et al. 2008; Anderson et al. 2011) and that the telescope does not track perfectly, resulting in a position-dependent low-frequency noise that can be modeled but will lead to greater uncertainty (because the model is never a perfect representation of the noise, and its parameters have their own errors that vary in magnitude with the measurement itself). The red noise is expected to stay constant or decrease very slowly with the number of transits and can be represented by a small X exponent. An intermediate scenario of "pink noise," as often used to describe sounds, is when the noise also decreases with

X but slower than for white noise. This is the realistic scenario considered here.

According to Greene et al. (2016), instrumental noise (introduced by decorrelation residuals) produces systematic noise floors that do not decrease when acquiring more photons (with a larger aperture and/or more integration time), like red noise. In *HST* WFC3 observations of GJ 1214 (Kreidberg et al. 2014), the errors obtained from 15 integrated transits are, however, in perfect agreement with a modeled "pure white noise," indicating a low noise (30 ppm) and decay close to $X^{-0.5}$. Tsiaras et al. (2016) reported the most precise transmission spectrum for a planet (55 Cancri e), with a single visit with *HST* WFC3 reaching 20–30 ppm precision over 25 channels. In the infrared with the *Spitzer Space Telescope*, values as low as 65 ppm have been achieved (Knutson et al. 2009). If we observe a large number of transits, the difference in frequency between the systematic effects and the orbit of the planet will approach the reduction in $X^{-0.5}$ of the white noise but without ever reaching it (pink noise). To suppose a fixed background (red) noise, as in Greene et al. (2016), implies neglecting this decrease. However, the fact that a noise floor better than 30 ppm has not been achieved yet is not due to the precision limit of instruments like *HST* WFC3, but rather to the fact that no one has ever accumulated enough high-S/N transits. Yet it is only by accumulating a large number of transits of the same object with *JWST* that we will know if the instruments can do better and measure the value of their background noise and the profile of its decay as a function of the number of transits. Note that this decay is very poorly
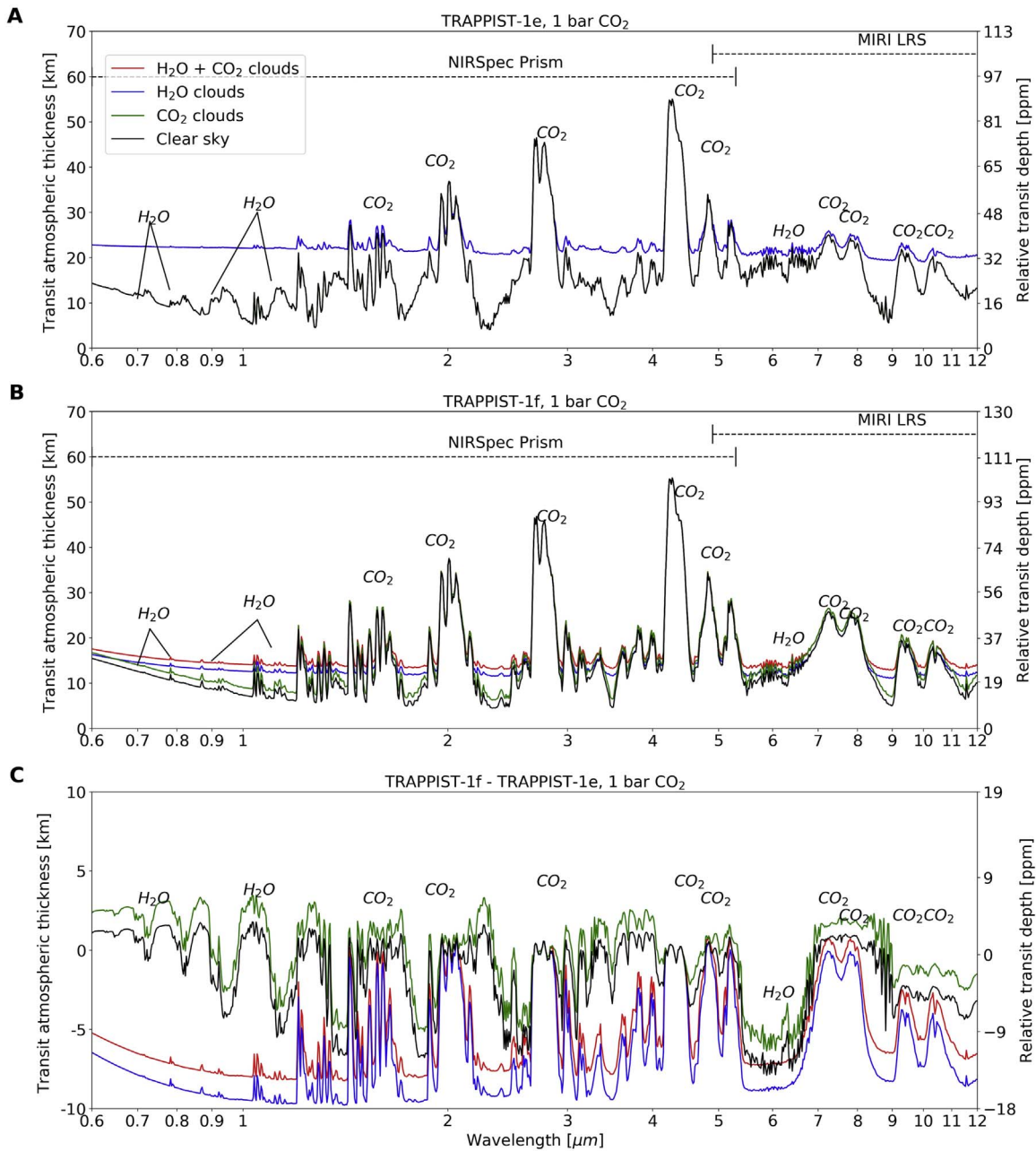
Figure 13. Simulated transmission spectra by *JWST* NIRSpec Prism and MIRI with $R = 300$ for aquaplanets (a) TRAPPIST-1e and (b) 1f with 1 bar of surface pressure of CO_2. Panel (c) shows differences between planetary spectra.

characterized in IR spectrophotometry, because to quantify it requires high-S/N observations and many transits observed.

Another way to estimate what we can expect to achieve as an estimated precision with *JWST* is to look at the accuracy reached by *Spitzer* or WFC3 at very high S/N in photometry rather than spectrophotometry. For HD 219134, Gillon et al. (2017a) obtained 20 ppm noise with only two transits at 4.5 μm, with a much less homogeneous InSb detector than the NIRSpec or WFC3 HgCdTe detector. Compared to the expected white noise, this produces red noise of less than 10 ppm, despite systematics of about 1000 ppm amplitude.

Figure 17 shows the S/N (left *y*-axis) and noise (right *y*-axis) for the CO_2 line at 4.3 μm of the modern Earth-like simulation as a function of the number of transits. We can see that when white noise is assumed (black curve), an S/N of 5 (5σ

detection) is reached in about 35 transits (see also Table 4). If the noise decreases slower ($-0.5 < X$ exponent <0.0) than for white noise, 5σ detection will require more transits. We show here that the noise exponent should not be greater than -0.4 to reach 5σ detection in less than 100 transits.

Deming et al. (2009) and Greene et al. (2016) assumed 1σ noise floors for NIRSpec Prism ($\lambda = 0.6$–5 μm) and MIRI LRS ($\lambda = 5.0$–11 μm) of 20 and 50 ppm, respectively. A 20 ppm noise floor for NIRSpec would correspond to the solid red line in Figure 17 of a noise depending on $X^{-0.2}$. However, we consider these values to be conservative. Indeed, unlike *HST* or *Spitzer*, the detector systematic behavior for exoplanet spectroscopy can be studied prior to the launch of *JWST*. This advantage, combined with the continuing improvement of data reduction techniques, should minimize the detector systematics
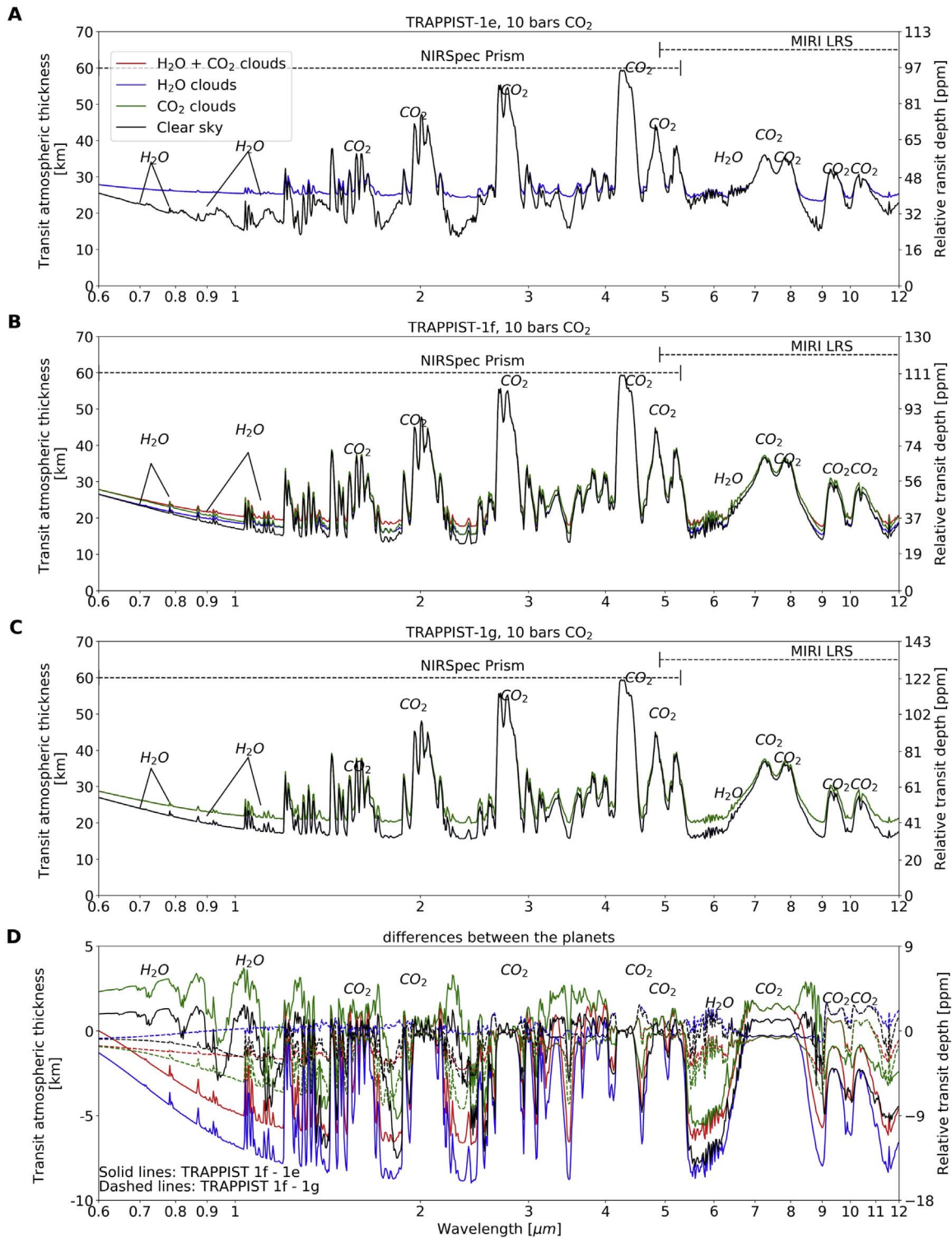
Figure 14. Simulated transmission spectra by *JWST* NIRSpec Prism and MIRI with $R = 300$ for aquaplanets (a) TRAPPIST-1e, (b) 1f, and (c) 1g with 10 bars of surface pressure of CO_2. Panel (d) shows differences between planetary spectra.

for *JWST*. Following the various arguments explained above, we consider half of the Deming et al. (2009) and Greene et al. (2016) noise floor values, i.e., 10 and 25 ppm 1σ optimistic noise floors for NIRSpec Prism and MIRI, respectively. Meanwhile, in this study, we consider the significance of a detection of an atmosphere (whatever the gas) at a 3σ confidence level but the detection of a specific biosignature gas such as O_2, O_3, CH_4, or even H_2O at 5σ. The a priori noise

floors should therefore be scaled accordingly by the factor of the confidence level. Table 9 shows the various noise floors as a function of the significant level considering either 20 and 50 ppm or 10 and 25 ppm for NIRSpec and MIRI, respectively.

Tables 4 (modern Earth atmosphere), 6 (Archean Earth atmosphere), and 8 (CO_2-rich atmospheres) show the number of transits needed to detect various gas features assuming white
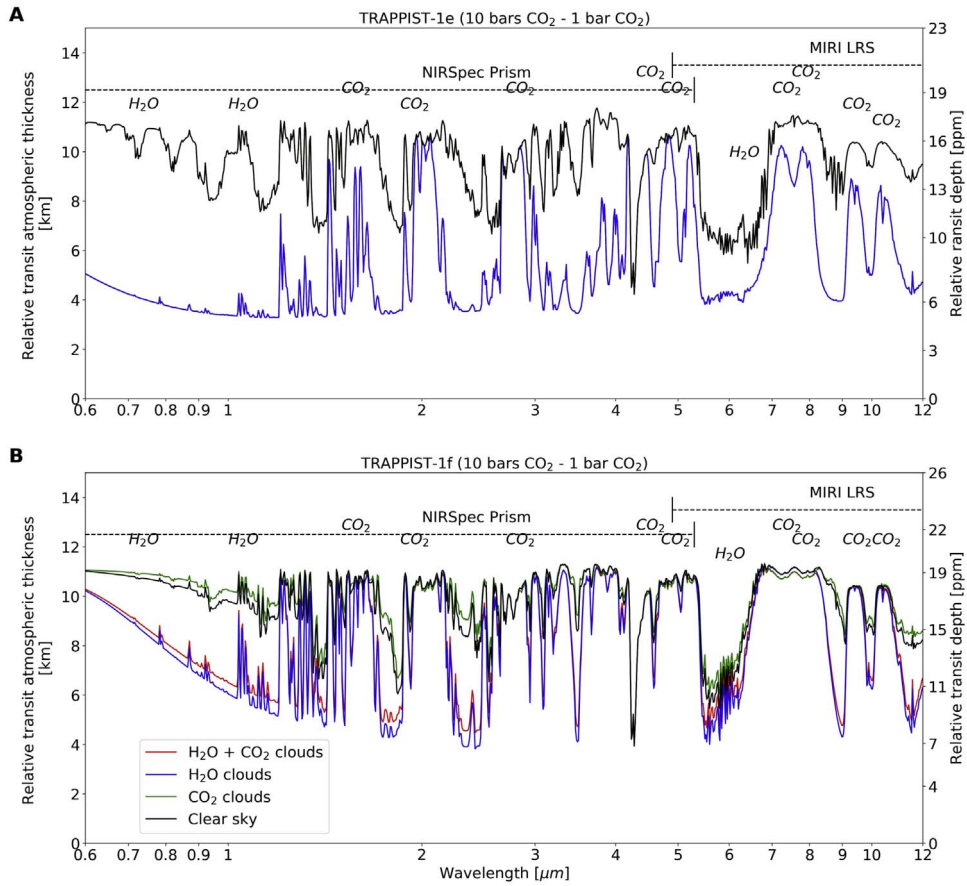
Figure 15. Difference between the spectra of the 10 and 1 bar CO_2 surface pressure for aquaplanets (a) TRAPPIST-1e and (b) 1f.

Table 8
Relative Transit Depth (ppm), S/N for One Transit (S/N-1), and Number of Transits to Achieve a 5σ and 3σ Detection for Various Spectral Lines of the CO_2-dominated Atmosphere

Planets Pressures	TRAPPIST-1e		TRAPPIST-1f		TRAPPIST-1g
	1 bar	10 bars	1 bar	10 bars	10 bars
Feature			H_2O 1.4 μm		
Depth (ppm)	3(18)	3(14)	4(12)	5(9)	5(10)
S/N-1	0.1(0.4)	0.1(0.3)	0.1(0.3)	0.1(0.2)	0.1(0.2)
No. of transits (5σ)	–	–	–	–	–
No. of transits (3σ)	−(54)	−(82)	–	−(82*)	–
Feature			CO_2 4.3 μm		
Depth (ppm)	61(86)	50(56)	80(96)	60(66)	67(74)
S/N-1	1.2(1.6)	0.9(1.1)	1.6(1.9)	1.2(1.3)	1.4(1.6)
No. of transits (5σ)	19(9)	28(22)	10(7)	17(15)	13(10)
No. of transits (3σ)	7(3)	10(8)	4(2)	6(5)	5(4)

Note. Numbers in parentheses are for clear sky only, while numbers without parentheses are the real values accounting for the impact of clouds. The hyphen represents the cases for which more than 100 integrated transits are needed, and the asterisks denote the values above the maximum number of transits observable per planet during the *JWST* nominal lifetime mentioned in Table 1.

noise and therefore without considering a noise floor. However, only the relative transit depth of the lines larger than the noise floor could be detected. For each gas feature allowing a

possible 3σ or 5σ detection, the relative transit depth should be compared with the estimated noise floor values of Table 9. If we assume the optimistic noise floors of Table 9, we estimate that an atmosphere can be detected by *JWST* using the CO_2 absorption at 4.3 μm for the following.

1. A modern Earth-like atmosphere with NIRSpec Prism from seven (TRAPPIST-1g) to 13 (TRAPPIST-1e[16]) transits at 3σ or 19 to 35 transits at 5σ.
2. An Archean Earth-like atmosphere with NIRSpec Prism from three (TRAPPIST-1g) to eight (TRAPPIST-1e) transits at 3σ or nine (TRAPPIST-1g) to 23 (TRAPPIST-1e) transits at 5σ.
3. A CO_2-rich atmosphere (1 and 10 bars) with NIRSpec Prism from five (TRAPPIST-1g) to 10 (TRAPPIST-1e) transits at 3σ or between 13 (TRAPPIST-1g) and 28 (TRAPPIST-1e) transits at 5σ.

Considering the conservative noise floors (Greene et al. 2016), we estimate that an atmosphere can be detected (only at 3σ) using the CO_2 absorption at 4.3 μm for the following.
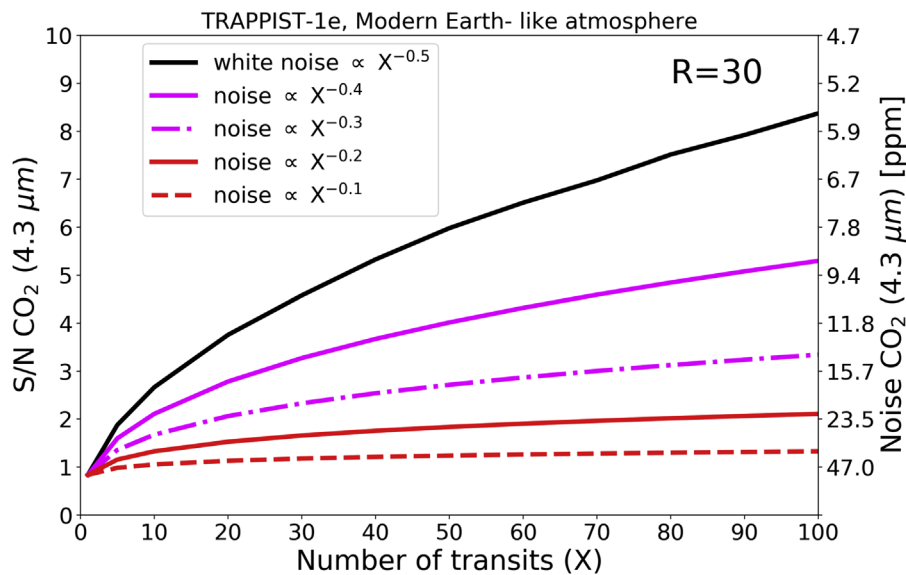
1. A modern Earth-like atmosphere with NIRSpec Prism from seven transits for TRAPPIST-1f and 1g; no detection for 1e.
2. An Archean Earth-like atmosphere with NIRSpec Prism for TRAPPIST-1g from three (TRAPPIST-1g) to eight transits (TRAPPIST-1e).

---

[16] Note that the relative transit depth of the CO_2 at 4.3 μm for TRAPPIST-1e (47 ppm) is just below the 5σ noise floor value of 50 ppm, but we assumed it was detectable considering the uncertainty of this calculation.

a)

b)

c)

d)
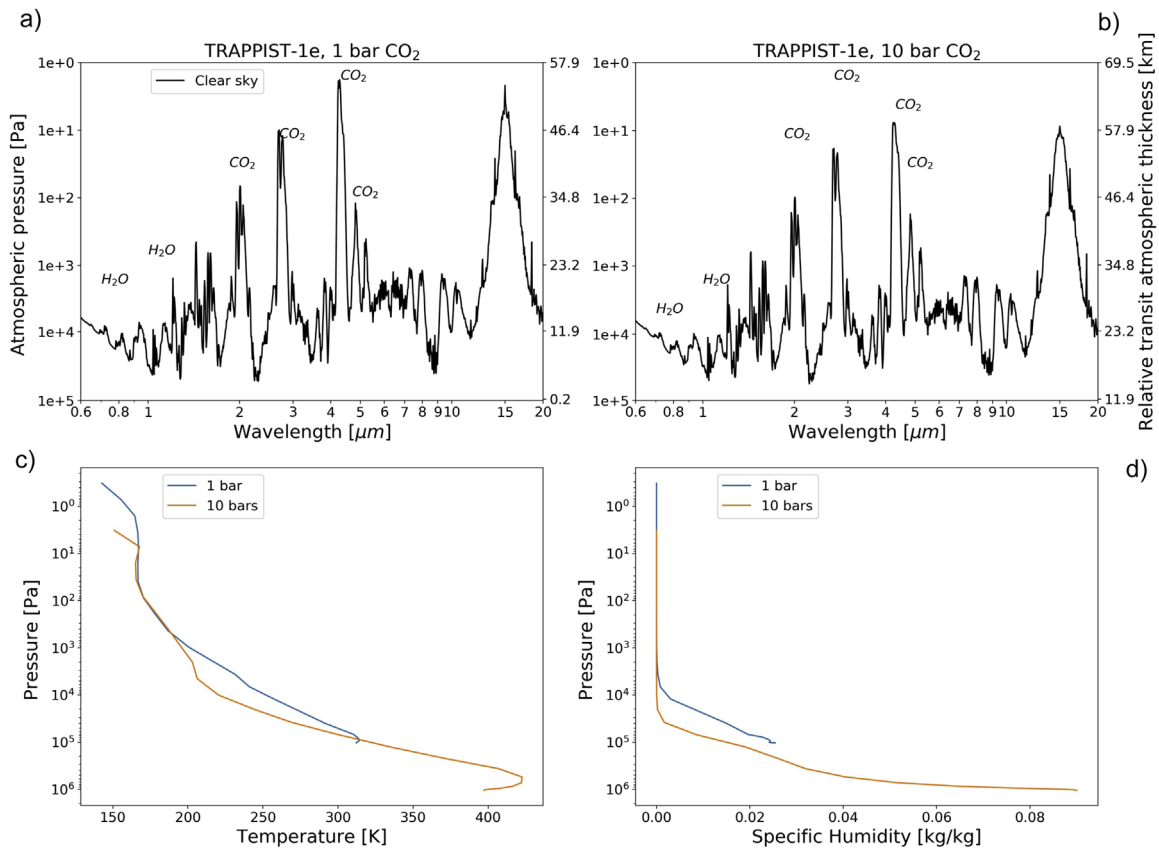
Figure 16. Simulated transmission spectra by *JWST* NIRSpec Prism and MIRI with $R = 300$ for the aquaplanet TRAPPIST-1e with (a) 1 and (b) 10 bars of CO_2 surface pressure. Also shown are (c) atmospheric temperature and (d) specific humidity, averaged at the terminator, as a function of the atmospheric pressure for 1 and 10 bar CO_2 surface pressures.

Figure 17. The S/N (left *y*-axis) and noise (right *y*-axis) for the CO_2 line at 4.3 μm of the modern Earth-like atmosphere simulated for *JWST* NIRSpec Prism at $R = 30$ as a function of the number of transits. White noise ($X^{-0.5}$, with *X* the number of transits) is represented by the black curve, while S/Ns with smaller *X* exponents are represented in pink (smaller increase of S/N with *X*) and red (almost constant with *X*) colors.

3. The CO_2-rich atmospheres (1 and 10 bars) with NIRSpec Prism are detectable from five (TRAPPIST-1f at 1 bar) to seven (TRAPPIST-1e at 1 bar) transits. The CO_2 transit depth for TRAPPIST-1e at 10 bars is below the noise floor.

Note that in the MIRI range, the higher value of the noise floors and/or the number of transits greater than 100 compromise the chance of detecting an atmosphere for the TRAPPIST-1 planets in the HZ with this instrument during the *JWST* lifetime. Concerning gases other than CO_2, such as O_2,
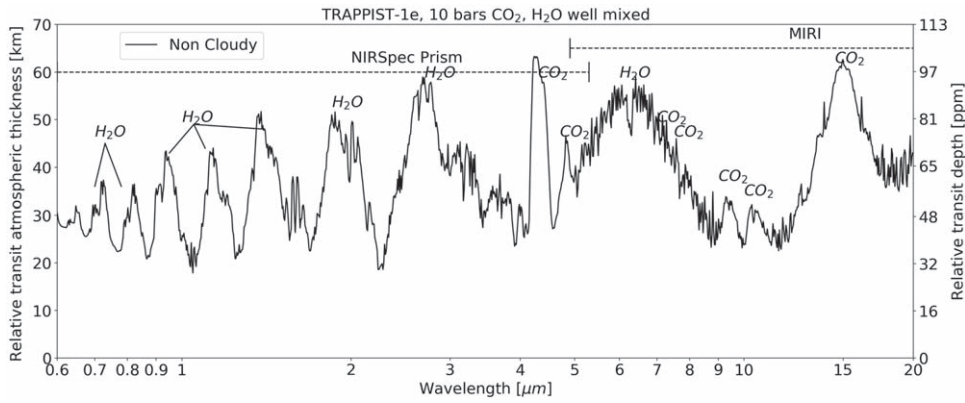
Figure 18. TRAPPIST-1e transmission spectrum for the 10 bars of CO_2 atmosphere for which H_2O has been forced to be vertically well mixed. In transmission spectroscopy, H_2O is much stronger when it is vertically well mixed than when it is confined near the surface.

Table 9
A Priori Noise Floors as a Function of the Detection Confidence Level from the Conservative and Optimistic 1σ Noise Floor Estimations (First and Second Column, Respectively, for Each Confidence Level)

	Noise Floors					
	1σ		3σ		5σ	
NIRSpec Prism	10	20	30	60	50	100
MIRI LRS	25	50	75	150	125	250

O_3, CH_4, or even H_2O, according to our simulated atmospheric scenarios, none of them are detectable during *JWST* at a 5σ confidence level, even for a photon-limited (white-noise) estimation.

6.2. Water Features

In this work, we have shown that water lines are challenging to detect from *JWST* transmission spectroscopy for habitable planets in the TRAPPIST-1 system (or an equivalent system of planets in the HZ of an (ultracool) M dwarf). The GCM simulations of those worlds show that water vapor stays confined in the lower atmosphere of the planets, namely in the troposphere. Nevertheless, layers near the surface are warmer, leading to an increasing infrared opacity of the water continuum and shallow lines. In this situation, even a small amount of well-mixed CO_2 in the atmosphere is enough to largely dominate over H_2O lines and hide them (like at 2.7 μm). As a result, none of the water vapor lines are larger than the presumed 3σ or 5σ noise floors (see Table 9). To have a large water mixing ratio through the whole atmospheric column would require either a moist greenhouse or runaway climate or a very low atmospheric pressure, in which case, the atmospheric cold trap is suppressed in particular in the substellar region, and the H_2O mixing ratio can remain high in the upper atmosphere (Turbet et al. 2016).

To represent how the confinement of H_2O near the surface affects its detectability, we have considered the following thought experiment for TRAPPIST-1e with 10 bars of CO_2, clear sky: the average atmospheric H_2O vapor mixing ratio (47%) confined below 20 km is now well mixed horizontally and vertically. While this may be a rather unrealistic scenario, it helps to understand how H_2O mixing through the atmosphere impacts the strength of the water lines. The resulting *JWST* transmission spectrum is shown in Figure 18. The H_2O lines

are now much stronger. In the NIRSpec range at a resolving power of 30, it is difficult to find an H_2O line not blended by CO_2, except for the shorter wavelengths. At 0.95 μm, the H_2O feature line reaches up to 32 ppm, and 89 transits would be needed to achieve a 5σ detection, but the transit depth is below the 50 ppm noise floor at 5σ. If one considers the significance of a 3σ detection, this absorption line would be detectable in 32 transits. Note that we do not include clouds here because we could not predict how clouds would form in such an atmosphere. However, they are expected to severely affect the detectability of the H_2O features. In general, this result demonstrates that the use of 3D climate models (taking self-consistently into account the effect of clouds and subsaturation) is crucial to correctly evaluate the detectability of condensible species such as water.

Water vapor in the atmosphere intrinsically leads to water cloud formation in either the liquid or ice phase. Clouds are formed where the majority of the water vapor is in a non-runaway atmosphere, and they partially block the transmitted light, flattening the spectrum, especially for H_2O. Well-mixed species such as CO_2 are less impacted because enough of them remains above the cloud deck.

Concerning emission spectroscopy, this technique is more sensitive to hot planets near the star (Morley et al. 2017). The hottest simulations we have performed are TRAPPIST-1e at 10 bars of CO_2. Figure 19 shows the emission spectrum for MIRI from 5 to 20 μm with $R = 300$ for the secondary eclipse. Below 5 μm, the contribution of the star removes the signal. The black curve shows the clear-sky spectrum, and the blue curve shows the cloudy-sky spectrum. While few strong H_2O lines are present here in the clear-sky case, once clouds are considered, those lines are flattened. The H_2O lines that are less impacted are near 20 μm, with a thermal contrast of 25 ppm, but this is much smaller than the noise in the MIRI and therefore will be hard to detect. Beyond 20 μm, clouds become more transparent; the planet/star contrast increases, and the noise increases dramatically as well. Therefore, it seems that emission spectroscopy with *JWST* is not helpful to detect H_2O lines, in agreement with Lustig-Yaeger et al. (2019).

Reflection spectroscopy may be a better option to probe water vapor lines because, contrary to the transmission spectroscopy for which the starlight is transmitted through the terminator of the planet, it could probe the disk of the planet where clouds could be absent in some regions at various phases. Also, reflection spectroscopy can probe the lowest level
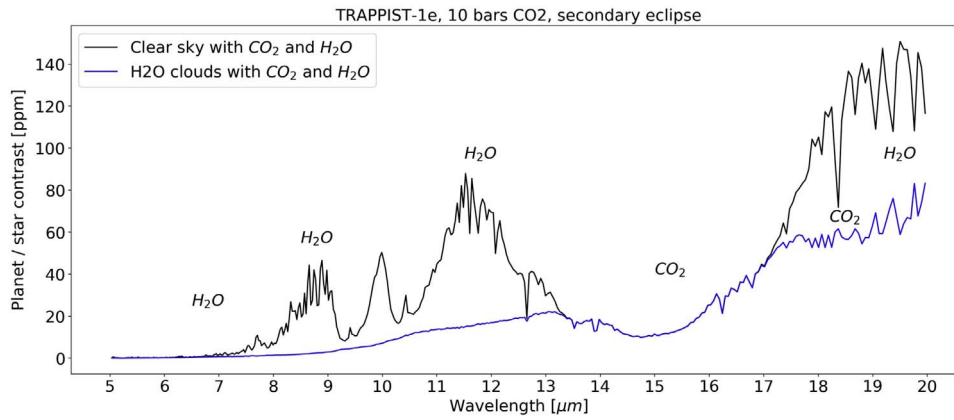
Figure 19. Emission spectrum from the secondary eclipse with MIRI ($R = 300$) for TRAPPIST-1e with an atmosphere consisting of a surface pressure of 10 bars of CO_2.

of the atmosphere, where most of the water resides. However, the small inner working angle of the instrument on future direct imaging missions such as *LUVOIR* or *HabEX* would prevent the observation of a compact system like TRAPPIST-1.

The combination of the two effects, (1) the water vapor confined in the low atmosphere and (2) the cloud opacities, implies that the detection of water vapor lines may be challenging for planets in the HZ of TRAPPIST-1 or an equivalent system.

7. Conclusions

In this work, we have successfully connected a global circulation model (LMD-G) to a 1D photochemical model (Atmos) and then applied a spectrum generator and noise model to estimate the detectability of gas species in a realistic set of possible atmospheres for the TRAPPIST-1 planets in the HZ. This has led to a consistent estimation of the cloud coverage, along with the atmospheric temperatures and water profiles of tidally locked planets around M dwarfs. However, the haze formation and photochemistry have been limited to the terminator region only, while a more consistent way would be to fully couple the GCM and the photochemical model. Also, no OHT has been considered (LMD-G does not have this feature yet), but that should not qualitatively impact our results. This coupling would lead to more clouds migrating toward the terminator with OHT enabled. These effects will be investigated in future studies.

We have seen that the Archean Earth-like atmospheres offer habitable conditions (an ice-free surface) for TRAPPIST-1e and 1f, while only TRAPPIST-1e is habitable if an atmosphere with boundary conditions based on the modern Earth is considered. The CO_2 atmospheres lead to very high surface temperatures. TRAPPIST-1e is fully habitable at 1 bar of CO_2, while TRAPPIST-1f is an eyeball planet (the TRAPPIST-1g atmosphere collapses at 1 bar of CO_2). At 10 bars of CO_2, the TRAPPIST-1e and 1f surface temperatures are so high that the oceans should evaporate, leading to desiccated planets. On the other hand, TRAPPIST-1g holds a few habitable ice-free spots near the substellar point.

Using the simulated *JWST* transmission spectroscopy, we found that an atmosphere with varying concentrations of CO_2 would be detectable for all habitable atmosphere configurations presented in this work in less than 15 transits at 3σ or less than 35 transits at 5σ with NIRSpec. Nevertheless, CO_2 is expected

to be an abundant gas in an exoplanet atmosphere owing to its large abundance in the rocky planet atmospheres of our solar system and its high molecular weight making it more resistant to atmospheric escape. This number of transit observations is reasonably achievable during the lifetime of *JWST*. Unfortunately, we did not find any gas other than CO_2 to be detectable during the *JWST* nominal lifetime or in less than 100 transits. Overall, it appears that NIRSpec performed better in terms of S/N and minimized the number of transits in comparison to MIRI. However, if hazes are detected on these planets, MIRI (in its shortest wavelengths between 5 and 10 μm) may perform better because the haze opacity is much lower than within the NIRSpec range. This study also suggests that it is very challenging to detect water lines for habitable planets orbiting ultracool dwarf stars such as TRAPPIST-1. Indeed, water mostly remains confined to the lower levels of the atmosphere, with higher IR opacity leading to shallow lines (well below the noise floor of the next space observatories), very often blended by stronger lines of the well-mixed CO_2. Water may be mixed through the entire atmospheric column if the planets are in a moist greenhouse state, but it will require a very high amount of GHG (greater than 10 bars), an instellation larger than the one received in the HZ, and/or a very thin atmosphere suppressing cold traps. In addition, water vapor in the atmosphere implies the formation of water clouds blocking the transmitted light and leading to the flattening of water lines.

Many effects are in competition to determine which of the three planets in the HZ offers the best chance of detection of an atmosphere. From TRAPPIST-1e to 1g, the planets get colder (decreasing the transit depth) but increase in size (increasing the transit depth). TRAPPIST-1e has the largest gravity (decreasing the transit depth), followed by 1g and 1f. Our simulations suggest that if a modern Earth-like atmosphere is present on the TRAPPIST-1 HZ planets, TRAPPIST-1e would be the most cloudy, while TRAPPIST-1f would be the most hazy for an Archean Earth-like atmosphere. Farther away, TRAPPIST-1g would have the lowest cloud and haze coverage. The atmospheric refraction also increases from TRAPPIST-1e to 1g, raising the continuum level to higher altitudes and therefore reducing the relative transit depths of the absorption lines. Finally, the frequency of observable transits during *JWST*'s nominal lifetime decreases from TRAPPIST-1e (85) to 1f (55) and 1g (42). Overall, it appears that TRAPPIST-1g offers the most favorable conditions for detection of an atmosphere, using the CO_2 line at 4.3 μm. We also found that

larger ice-free surfaces lead to more clouds formed, themselves significantly hiding habitability markers (such as water vapor absorption lines). It is then possible that habitability would be more feasibly detectable if the planet were habitable locally rather than globally.

Software: Atmos (Arney et al. 2016), LMD-G (Wordsworth et al. 2011), PSG (Villanueva et al. 2018).

ORCID iDs

Thomas J. Fauchez ⃝ https://orcid.org/0000-0002-5967-9631
Eric T. Wolf ⃝ https://orcid.org/0000-0002-7188-1648
Giada Arney ⃝ https://orcid.org/0000-0001-6285-267X
Ravi K. Kopparapu ⃝ https://orcid.org/0000-0002-5893-2471
Andrew Lincowski ⃝ https://orcid.org/0000-0003-0429-9487
Avi Mandell ⃝ https://orcid.org/0000-0002-8119-3355
Julien de Wit ⃝ https://orcid.org/0000-0003-2415-2191
Daria Pidhorodetska ⃝ https://orcid.org/0000-0001-9771-7953
Shawn D. Domagal-Goldman ⃝ https://orcid.org/0000-0003-0354-9325
Kevin B. Stevenson ⃝ https://orcid.org/0000-0002-7352-7941

References

Anderson, D. R., Smith, A. M. S., Lanotte, A. A., et al. 2011, MNRAS, 416, 2108
Anglada-Escudé, G., Amado, P. J., Barnes, J., et al. 2016, Natur, 536, 437
Arney, G., Domagal-Goldman, S. D., Meadows, V. S., et al. 2016, AsBio, 16, 873
Arney, G. N., Meadows, V. S., Domagal-Goldman, S. D., et al. 2017, ApJ, 836, 49
Barnes, R. 2017, CeMDA, 129, 509
Barstow, J. K., & Irwin, P. G. J. 2016, MNRAS, 461, L92
Batalha, N. E., Lewis, N. K., Line, M. R., Valenti, J., & Stevenson, K. 2018, ApJL, 856, L34
Berta-Thompson, Z. K., Irwin, J., Charbonneau, D., et al. 2015, Natur, 527, 204
Bolmont, E., Selsis, F., Owen, J. E., et al. 2017, MNRAS, 464, 3728
Bonfils, X., Astudillo-Defru, N., Díaz, R., et al. 2018, A&A, 613, A25
Boucher, O., Le Treut, H., & Baker, M. B. 1995, JGR, 100, 16395
Bourrier, V., de Wit, J., Bolmont, E., et al. 2017, AJ, 154, 121
Burkholder, S. P. S., Abbatt, J., & Barker, J. R. 2015, Chemical Kinetics and Photochemical Data for Use in Atmospheric Studies, Technical Report 18, Jet Propulsion Laboratory, Pasadena, http://jpldataeval.jpl.nasa.gov
Carone, L., Keppens, R., & Decin, L. 2014, MNRAS, 445, 930
Carone, L., Keppens, R., & Decin, L. 2015, MNRAS, 453, 2412
Carone, L., Keppens, R., Decin, L., & Henning, T. 2018, MNRAS, 473, 4672
Charnay, B., Forget, F., Wordsworth, R., et al. 2013, JGRD, 118, 10414
Charnay, B., Meadows, V., & Leconte, J. 2015a, ApJ, 813, 15
Charnay, B., Meadows, V., Misra, A., Leconte, J., & Arney, G. 2015b, ApJL, 813, L1

Chen, H., Wolf, E. T., Kopparapu, R., Domagal-Goldman, S., & Horton, D. E. 2018, ApJL, 868, L6
de Wit, J., & Seager, S. 2013, Sci, 342, 1473
de Wit, J., Wakeford, H. R., Gillon, M., et al. 2016, Natur, 537, 69EP
de Wit, J., Wakeford, H. R., Lewis, N. K., et al. 2018, NatAs, 2, 214
Del Genio, A. D., Way, M. J., Amundsen, D. S., et al. 2019, AsBio, 19, 99
Deming, D., Seager, S., Winn, J., et al. 2009, PASP, 121, 952
Dong, C., Jin, M., Lingam, M., et al. 2018, PNAS, 115, 260
Forget, F., Hourdin, F., Fournier, R., et al. 1999, JGR, 104, 24155
Forget, F., & Pierrehumbert, R. T. 1997, Sci, 278, 1273
Forget, F., Wordsworth, R., Millour, E., et al. 2013, Icar, 222, 81
Gavilan, L., Broch, L., Carrasco, N., Fleury, B., & Vettier, L. 2017, ApJL, 848, L5
Gillon, M., Demory, B.-O., Van Grootel, V., et al. 2017a, NatAs, 1, 0056
Gillon, M., Jehin, E., Lederer, S. M., et al. 2016, Natur, 533, 221
Gillon, M., Triaud, A. H. M. J., Demory, B.-O., et al. 2017b, Natur, 542, 456
Greene, T. P., Line, M. R., Montero, C., et al. 2016, ApJ, 817, 17
Grenfell, J., Gebauer, S. V., Paris, P., Godolt, M., & Rauer, H. 2014, P&SS, 98, 66
Grimm, S. L., Demory, B.-O., Gillon, M., et al. 2018, A&A, 613, A68
Haberle, R. M., Zahnle, K., & Barlow, N. 2017, LPICo, 2014, 3022
Hansen, G. B., Warren, S. G., & Leovy, C. B. 1991, Optical Properties of CO2 Ice and CO2 Snow from Ultraviolet to Infrared: Application to Frost Deposits and Clouds on Mars, NASA Technical Report SEE N92-10728 01-91, NASA
Hansen, J. E., & Travis, L. D. 1974, SSRv, 16, 527
Harman, C. E., Felton, R., Hu, R., et al. 2018, ApJ, 866, 56
Hourdin, F., Musat, I., Bony, S., et al. 2006, ClDy, 27, 787
Hu, Y., & Yang, J. 2014, PNAS, 111, 629
Joshi, M. 2003, AsBio, 3, 415
Joshi, M. M., & Haberle, R. M. 2012, AsBio, 12, 3
Kaltenegger, L., & Traub, W. A. 2009, ApJ, 698, 519
Kasting, J. F., Whitmire, D. P., & Reynolds, R. T. 1993, Icar, 101, 108
Khare, B. N., Sagan, C., Arakawa, E. T., et al. 1984, Icar, 60, 127
Kite, E. S. 2019, SSRv, 215, 10
Kitzmann, D. 2017, A&A, 600, A111
Knutson, H. A., Charbonneau, D., Allen, L. E., Burrows, A., & Megeath, S. T. 2008, ApJ, 673, 526
Knutson, H. A., Charbonneau, D., Cowan, N. B., et al. 2009, ApJ, 703, 769
Kopparapu, R. K., Ramirez, R., Kasting, J. F., et al. 2013, ApJ, 765, 131
Kopparapu, R. K., Wolf, E. T., Arney, G., et al. 2017, ApJ, 845, 5
Kreidberg, L., Bean, J. L., Désert, J.-M., et al. 2014, Natur, 505, 69
Lacis, A. A., & Oinas, V. 1991, JGR, 96, 9027
Lammer, H., Bredehöft, J. H., Coustenis, A., et al. 2009, A&ARv, 17, 181
Leconte, J., Forget, F., Charnay, B., Wordsworth, R., & Pottier, A. 2013a, Natur, 504, 268
Leconte, J., Forget, F., Charnay, B., et al. 2013b, A&A, 554, A69
Leconte, J., Wu, H., Menou, K., & Murray, N. 2015, Sci, 347, 632
Lincowski, A. P., Meadows, V. S., Crisp, D., et al. 2018, ApJ, 867, 76
Line, M. R., & Parmentier, V. 2016, ApJ, 820, 78
Luger, R., Sestovic, M., Kruse, E., et al. 2017, NatAs, 1, 0129
Lustig-Yaeger, J., Meadows, V. S., & Lincowski, A. P. 2019, AJ, 158, 27
Massie, S. T., & Hervig, M. 2013, JQSRT, 130, 373
Meadows, V. S., Arney, G. N., Schwieterman, E. W., et al. 2018, AsBio, 18, 133
Meadows, V. S., & Crisp, D. 1996, JGR, 101, 4595
Merlis, T. M., & Schneider, T. 2010, JAMES, 2, 13
Moran, S. E., Hörst, S. M., Batalha, N. E., Lewis, N. K., & Wakeford, H. R. 2018, AJ, 156, 252
Morley, C. V., Kreidberg, L., Rustamkulov, Z., Robinson, T., & Fortney, J. J. 2017, ApJ, 850, 121
Nikolov, N., Sing, D. K., Burrows, A. S., et al. 2015, MNRAS, 447, 463
O'Malley-James, J. T., & Kaltenegger, L. 2017, MNRAS: Lett., 469, L26
Perrin, M. Y., & Hartmann, J. M. 1989, JQSRT, 42, 311
Pierrehumbert, R. T. 1995, JAtS, 52, 1784
Quintana, E. V., Barclay, T., Raymond, S. N., et al. 2014, Sci, 344, 277
Rajpurohit, A. S., Reylé, C., Allard, F., et al. 2013, A&A, 556, A15
Richard, C., Gordon, I., Rothman, L., et al. 2012, JQSRT, 113, 1276
Rossow, W. B. 1978, Icar, 36, 1
Rothman, L., Gordon, I., Barbe, A., et al. 2009, JQSRT, 110, 533
Rothman, L., Gordon, I., Barber, R., et al. 2010, JQSRT, 111, 2139
Segura, A., Krelove, K., Kasting, J. F., et al. 2003, AsBio, 3, 689
Selsis, F., Kasting, J. F., Levrard, B., et al. 2007, A&A, 476, 1373
Shields, A. L., Meadows, V. S., Bitz, C. M., et al. 2013, AsBio, 13, 715
Showman, A. P., & Polvani, L. M. 2011, ApJ, 738, 71
Sing, D. K., Fortney, J. J., Nikolov, N., et al. 2016, Natur, 529, 59

Snellen, I. A. G., de Kok, R. J., le Poole, R., Brogi, M., & Birkby, J. 2013, ApJ, 764, 182

Toon, O. B., McKay, C. P., Ackerman, T. P., & Santhanam, K. 1989, JGR, 94, 16287

Tsiaras, A., Rocchetto, M., Waldmann, I. P., et al. 2016, ApJ, 820, 99

Turbet, M., Bolmont, E., Leconte, J., et al. 2018, A&A, 612, A86

Turbet, M., Forget, F., Head, J. W., & Wordsworth, R. 2017a, Icar, 288, 10

Turbet, M., Forget, F., Leconte, J., Charnay, B., & Tobie, G. 2017b, E&PSL, 476, 11

Turbet, M., Leconte, J., Selsis, F., et al. 2016, A&A, 596, A112

Vida, K., & Roettenbacher, R. M. 2018, A&A, 616, A163

Villanueva, G. L., Smith, M. D., Protopapa, S., Faggi, S., & Mandell, A. M. 2018, JQSRT, 217, 86

von Paris, P., Selsis, F., Kitzmann, D., & Rauer, H. 2013, AsBio, 13, 899

Wakeford, H. R., Visscher, C., Lewis, N. K., et al. 2017, MNRAS, 464, 4247

Warren, S. G. 1984, AnGla, 5, 177

Warren, S. G., & Wiscombe, W. J. 1980, JAtS, 37, 2734

Way, M. J., Aleinov, I., Amundsen, D. S., et al. 2017, ApJS, 231, 12

Wheatley, P. J., Louden, T., Bourrier, V., Ehrenreich, D., & Gillon, M. 2017, MNRAS: Lett., 465, L74

Winn, J. N. 2010, arXiv:1001.2010

Wolf, E. T. 2017, ApJL, 839, L1

Wolf, E. T., & Toon, O. B. 2015, JGRD, 120, 5775

Wordsworth, R., Forget, F., & Eymet, V. 2010, Icar, 210, 992

Wordsworth, R., Forget, F., Millour, E., et al. 2013, Icar, 222, 1

Wordsworth, R. D., Forget, F., Selsis, F., et al. 2011, ApJL, 733, L48

Wordsworth, R. D., Kerber, L., Pierrehumbert, R. T., Forget, F., & Head, J. W. 2015, JGRE, 120, 1201

Yang, J., Boué, G., Fabrycky, D. C., & Abbot, D. S. 2014, ApJL, 787, L2

Yang, J., Cowan, N. B., & Abbot, D. S. 2013, ApJL, 771, L45

Zahnle, K., & Schaefer, L. B. F. 2010, Cold Spring Harb Perspect Biol, 2, 17

Zmuidzinas, J. 2003, ApOpt, 42, 4989